

# Stratified multifractal magnetization and surface geomagnetic fields—II. Multifractal analysis and simulations

S. Pecknold,<sup>1</sup> S. Lovejoy<sup>1</sup> and D. Schertzer<sup>2,3</sup>

<sup>1</sup>Department of Physics, McGill University, 3600 University Street, Montréal, Québec, Canada, H3A 2T8. E-mail: lovejoy@physics.mcgill.ca

<sup>2</sup>LMM (CNRS-URA 229) Boite 162, Université Pierre et Marie Curie, 4 Place Jussieu, Paris 75252 Cedex 05, France

<sup>3</sup>Mathematical Sciences, Clemens University, Box 341907, Clemens, SC 29634–1907, USA

Accepted 2000 September 29. Received 2000 September 29; in original form 1997 July 22

## SUMMARY

In Paper I, we showed how anisotropic scaling spectral (second-order) models of the magnetization ( $\mathbf{M}$ ) were realistic at both high- and intermediate-wavenumber regimes of the surface magnetic field ( $\mathbf{B}$ ). However, in order to produce full stochastic  $\mathbf{M}$  and surface  $\mathbf{B}$  models, we need assumptions about statistical moments other than second order. The usual approach is to assume quasi-Gaussian statistics so that all the statistical moments are scaling according to a single exponent. The corresponding fields are monofractal. All structures—both weak and strong—have the same unique fractal dimension, there are no strong anomalies and there are no intermittent transitions from one strata or region to another; such assumptions are quite unrealistic. Using seven surface  $\mathbf{B}$  surveys, we show that the data are, on the contrary, multifractal, and we characterize their multifractal parameters in both the high- and intermediate-wavenumber regimes with the help of universal multifractal exponents. Using anisotropic (stratified) multifractal models, we deduce the  $\mathbf{M}$  statistics and produce  $\mathbf{M}$  and surface  $\mathbf{B}$  simulations with all statistical exponents quite near to those of the observed surface  $\mathbf{B}$  field; they are also visually realistic, showing anomalies at all scales. Finally, we analyse the horizontal anisotropy of the surface  $\mathbf{B}$  fields and use this to infer the  $\mathbf{M}$  statistics. This enables us to produce anisotropic 3-D  $\mathbf{M}$ ,  $\mathbf{B}$  models with more realistic texture and morphology of structures. We conclude that both multifractality and scaling anisotropy are indispensable for realistic geophysical models.

**Key words:** fractals, geomagnetism, multifractal analyses.

## 1 INTRODUCTION

In Paper I of this series, we argued that scaling models of geophysical fields were necessary in order to account for the ubiquity of fractal structures spanning wide ranges of scale. However, to be realistic we saw that at the very least the vertical stratification had to be accounted for, that is, that the scaling must be anisotropic. In particular, while anisotropic scaling models of the magnetization ( $\mathbf{M}$ ) generically lead to scaling, ‘red noise’ intermediate-range surface magnetic ( $\mathbf{B}$ ) fields; isotropic (self-similar) models, on the other hand, imply no intermediate range and virtually no variability at horizontal wavenumbers less than the Curie wavenumber [inverse Curie depth  $(10 \text{ km})^{-1}$  to  $(100 \text{ km})^{-1}$ ]. Although scaling stratification is enough to make realistic second-order (spectral) models of  $\mathbf{M}$  and surface  $\mathbf{B}$ , by itself the spectrum is generally not enough to define a complete stochastic model. The main exception—which is all too often invoked—is when the statistics are assumed to be quasi-Gaussian, in which case all the statistics are defined from the

spectrum. However, there are several strong arguments against quasi-Gaussian statistics. At a purely qualitative level, they involve small fluctuations, hence quasi-Gaussian processes would not produce very interesting structures (such as strong magnetic or other ‘anomalies’), there would be no sudden ‘intermittent’ transitions from one strata to another or from one geological province to another, and the spectral exponents estimated from single realizations (e.g. single boreholes) would all have nearly the same values. In short, a quasi-Gaussian process would not be acceptable on basic qualitative empirical grounds. In addition to these qualitative arguments, many studies of marginal probability distributions of geophysical quantities (starting with de Wijs 1951; see Pilkington & Todoeschuk 1993 for susceptibilities) have produced a log-normal phenomenology of geophysical fluctuations, that is, they have found statistics close to long-tailed log-normal distributions, proving that rare large events/gradients/values are far more common than quasi-Gaussian statistics would allow. Although it is now known that strict log-normality is incompatible with scaling,

quasi-log-normality is on the contrary an attractive, stable ('universal') multifractal behaviour, hence it is indeed *prima facie* evidence for multifractality. This incompatibility is due to the singular small-scale limit in multifractals, which gives rise to the divergence of high-order statistical moments, hence log-normality breaks down for the extremes (it will underestimate them) (see Schertzer & Lovejoy 1987, 1992, 1994).

Scaling quasi-Gaussian processes are the generalizations of Brownian motions called fractional Brownian motion (fBM) and are obtained by fractionally integrating (power-law convolving, power-law filtering) Gaussian white noise. Since convolutions are linear operations, such processes are 'additive'. They are also 'monofractal' since—taking the example of an fBM topography (as originally proposed by Mandelbrot 1977)—all the various topographic level sets (constant altitude sets) have identical fractal dimensions. Other (additive) generalizations of Brownian motion can be obtained by fractionally integrating various Levy noises, but these are still essentially monofractal, and have such strong intermittency that their variances diverge (their standard spectra are therefore not defined).

Although due to its apparent simplicity it is tempting to reduce the properties of a scaling process to a unique exponent—hence to a unique fractal dimension—developments in non-linear physics throughout the 1980s (particularly in turbulence theory) have shown that this is simplistic and that scaling processes are generally multifractal involving an infinite number of fractal sets, each with different fractal dimensions. Indeed, since scale-invariant fields generally define an infinite number of scale-invariant (fractal) sets—for example, one for each threshold level—it would be a miracle if all the infinite number of fractal sets each had exactly the same fractal dimension. In turbulence, multifractality is now so well established both theoretically (cascade processes) and empirically (high Reynolds's number experiments) that the debate is no longer about multifractals *per se*, but rather about the exact form of the scaling exponent function (see Schertzer *et al.* 1995 and Schertzer & Lovejoy 1997 for more details on the debate). In solid earth geophysics, probably the most convincing empirical evidence for multifractality is that of the topography (Lovejoy & Schertzer 1990; Lavallée *et al.* 1993; Weissel & Pratson 1994), although Marsan & Bean (1999) have shown that gamma emission and seismic velocity are also multifractal and Lovejoy *et al.* (2001a) show that surface gravity is also multifractal over various ranges.

The objectives of this paper are therefore first to show that the surface **B** field is indeed multifractal, and to characterize the infinite hierarchy of exponents by three universal multifractal parameters. We then use this information—with the help of stochastic (stratified, anisotropic) multifractal **M** models to deduce the **M** statistics and show how to make realistic **M**, **B** models that include scaling horizontal anisotropy. These models fit all the available statistical observations of surface **B** and volume **M** at all ranges of scales and all levels of intensity (e.g. all moments, not just second order).

## 2 MULTIFRACTALS AND UNIVERSAL MULTIFRACTALS

Multifractal fields have scaling properties characterized by a scaling exponent function. Thus, if we consider the probability of finding a field value  $\varepsilon_\lambda$  exceeding a given scale-dependent threshold  $\lambda^\gamma$ , where  $\lambda$  is the scale ratio, we find that this probability,  $\Pr(\varepsilon_\lambda > \lambda^\gamma)$ , can be related to the order of singularity  $\gamma$

that characterizes this threshold by

$$\Pr(\varepsilon_\lambda > \lambda^\gamma) \approx \lambda^{-c(\gamma)}, \quad (1)$$

$$\gamma = \log \varepsilon_\lambda / \log \lambda,$$

where the co-dimension function,  $c(\gamma)$ , describes the *sparseness* of the field intensities (Schertzer & Lovejoy 1987). When  $c(\gamma)$  is less than the dimension of space ( $d$ ) it can be given a geometric interpretation since  $D(\gamma) = d - c(\gamma)$  is the fractal dimension of the set of points where  $\varepsilon_\lambda$  exceeds  $\lambda^\gamma$ .

An equivalent statistical description of the multifractal  $\varepsilon_\lambda$  may be made in terms of the moment scaling function,  $K(q)$  (not to be confused with the horizontal wavenumber), which is defined as

$$\langle \varepsilon_\lambda^q \rangle \approx \lambda^{K(q)}. \quad (2)$$

This gives the scaling behaviour of each moment  $q$  of the field. In real systems this multiscaling behaviour [which implies a non-linear convex  $K(q)$ ] holds only over some finite range of scales. These, however, can be quite large; in the case of the atmosphere, noted above, the ratio of largest to smallest scale may be of the order of  $10^9$ – $10^{10}$  (from planetary scale to viscous dissipation scale; see e.g. Sachs *et al.* 2001; Lovejoy *et al.* 2001a).

These scaling exponent functions allow a complete characterization of the statistics of the field. They are nevertheless difficult to handle since they represent an infinite hierarchy of parameters— $K(q)$  can be an arbitrary convex function. We wish to find an expression for one or both of these functions that will enable us to describe the scaling in a fairly simple form with a small number of parameters. In order to do this, we note that many geophysical systems involve turbulence, which has long been regarded as arising from cascade processes (Richardson 1922). Many explicit cascade models have been developed where a quantity such as energy flux (for atmospheric turbulence) is injected at large scales and is cascaded to smaller and smaller scales via multiplicative modulations.

At first sight, the infinity of multifractal exponents makes them apparently unmanageable: theoretically a model would require an infinite number of parameters, and empirically we would also need estimates of an infinite number. Fortunately, stable, attractive universality classes exist for multifractal processes. This means that independently of many of the dynamical details, physically relevant multifractal processes are likely to depend on just three fundamental parameters (Schertzer & Lovejoy 1987, 1991). For the recent debate about strong versus weak universality, see Schertzer *et al.* (1995) and Schertzer & Lovejoy (1997). This means that under quite general conditions involving scaling non-linear cascade-like dynamics (that is, even in the absence of true turbulence), the generic result is believed to be 'universal' multifractals (Schertzer & Lovejoy 1987), where the  $K(q)$  function is given by

$$K(q) = \frac{C_1}{\alpha - 1} (q^\alpha - q), \quad \alpha \neq 1, \quad (3)$$

$$K(q) = C_1 q \log q, \quad \alpha = 1,$$

where  $0 < \alpha \leq 2$ . The parameter  $C_1$  is the co-dimension of the mean of the field, characterizing the sparseness of the set of points that make the dominant contribution to the mean of the field. The Lévy index  $\alpha$  characterizes the degree of multifractality (Schertzer & Lovejoy 1987). As  $\alpha \rightarrow 0$ ,  $K(q)$  becomes

linear and we obtain the monofractal  $\beta$ -model (Novikov & Stewart 1964; Yaglom 1966; Mandelbrot 1974; Frisch *et al.* 1978), where the field may be described by a single fractal dimension; the maximum value  $\alpha=2$  corresponds to the well-known case of the log-normal multifractal (this is actually a misnomer—due to divergence of high-order moments, the distribution will only be approximately log-normal).

Although some of the technical details are non-trivial and have led to debate about multifractal universality (see e.g. Schertzer & Lovejoy 1997), the basic theoretical arguments are straightforward. First, Schertzer & Lovejoy (1987) have shown that multifractal cascades are generic multifractal processes (i.e. they generally obey eq. 1). This implies that  $\log \varepsilon_\lambda$  (the cascade ‘generator’) is an additive process, hence the (generalized) central limit theorem implies that the logs tend to a normal or Levy distribution and hence that the process  $\varepsilon_\lambda$  tends to a log-normal or log-Levy process. These universal multifractals have now been shown to describe a large number of geophysical and other systems [see Lovejoy & Schertzer (1995) for a recent review and Lovejoy & Schertzer (1998, 1999) for a discussion of the theoretical framework of ‘stochastic chaos’].

The description of  $\varepsilon_\lambda$  in terms of statistical moments and the description in terms of probabilities are linked since the latter are related by a Mellin transformation. For their exponents [ $K(q)$  and  $c(\gamma)$ ], the Mellin transformation reduces to a Legendre transformation (Parisi & Frisch 1985),

$$c(\gamma) = \max_q / (q\gamma - K(q)),$$

$$K(q) = \max_\gamma (q\gamma - c(\gamma)). \quad (4a)$$

This Legendre transformation shows that there is a one-to-one relation between the field values (the singularities) and moments:  $q = c'(\gamma)$ ,  $\gamma = K'(q)$ . Applying eq. (4a) to the  $K(q)$  in eq. (3) yields the corresponding co-dimension function  $c(\gamma)$ ,

$$c(\gamma) = C_1 \left( \frac{\gamma}{C_1 \alpha'} + \frac{1}{\alpha} \right)^{\alpha'}, \quad (4b)$$

where  $\alpha'$  is defined by  $(1/\alpha) + (1/\alpha') = 1$ . The precise meaning of the above interpretation of  $C_1$  as the co-dimension of the set giving the dominant contribution to the mean is that  $\gamma = K'(1)$  is the corresponding singularity and  $c(K'(1)) = C_1$ . It turns out that for conservative multifractals,  $K(1) = 0$ , so that we also have from eq. (4a)  $C_1 = K'(1)$ , hence  $c(C_1) = C_1$  is a fixed point.

Unfortunately, we can rarely, if ever, directly observe the scale-by-scale conserved ( $\varepsilon_\lambda$ ) fields that are the direct outcome of the cascade process. Most observable fields ( $f_\lambda$ ) are instead related to the fluxes via scaling relations involving a third exponent  $H$  of the following type:

$$|\Delta f_\lambda| \approx \varepsilon_\lambda \lambda^{-H}, \quad (5)$$

whereas most multifractal analysis techniques require the analysis of fluxes ( $\varepsilon$ ). In the fractionally integrated flux (FIF) models, the  $\lambda^{-H}$  (linear) scaling term is modelled by a fractional integration (power-law filter) of  $\varepsilon_\lambda$  to obtain  $f_\lambda$ . Hence, to obtain the conservative process, we invert this by differentiating/integrating by the same order [Fourier space filtering by  $|k|^H$ —see the next section and see Schertzer *et al.* (1997) for more on this FIF model].

### 3 ESTIMATING THE MULTIFRACTAL PARAMETERS

In order to estimate the universal multifractal parameters  $\alpha$ ,  $C_1$ ,  $H$  of a multifractal field, we will employ a ‘bootstrap’ technique in which we first obtain a nearly conservative field that allows us to obtain rough estimates of the parameters. We then use the  $H$  estimate to obtain a more accurate conservative field, and hence refined estimates. In order to see how this works, consider the estimation of  $\alpha$  and  $C_1$  from a conservative field. The most powerful technique is the double trace moment, or DTM, technique (Lavallée *et al.* 1992, 1993) in which the field  $\varepsilon$  at the finest resolution is first raised to the power  $\eta$  and then integrated (or degraded in resolution or ‘dressed’) up to a scale  $\lambda$ . This renormalized field will then be described by its own moment scaling function,  $K(q, \eta)$ . The relation between  $K(q, \eta)$  and the usual statistical scaling exponent  $K(q)$  is (Lavallée *et al.* 1992)

$$K(q, \eta) = K(q\eta) - qK(\eta). \quad (6)$$

For the case where the process is a universal multifractal we have (applying eq. 6 to eq. 3)

$$K(q, \eta) = \eta^\alpha K(q) = \eta^\alpha \frac{C_1}{\alpha - 1} (q^\alpha - q), \quad \alpha \neq 1. \quad (7)$$

The scaling exponent in this case has two factors; one depends only on the universal parameter  $\alpha$ . By fixing  $q$  and varying  $\eta$ , we can determine the value of the parameter  $\alpha$  directly and then deduce  $C_1$  from  $K(q)$ . By plotting  $K(q, \eta)$  versus  $\eta$  on a double logarithmic plot, we can determine the value of  $\alpha$  from the slope of the line. Using this estimate of  $\alpha$  and the value of  $q$ , we can deduce the value of  $C_1$  (for example, from the intercept of the line with  $\eta=1$ ). The only complication is that eqs (3) and (7) will break down for sufficiently high-order moments when the statistics are dominated by a single extreme value (this corresponds to multifractal phase transitions; these can be of either first or second order; see details in Schertzer & Lovejoy 1994). It will also generally break down for extreme low values of  $q\eta$  due either to the presence of noise in the data or to discretization effects (the true number of very low gradients of the field is often not easy to estimate accurately).

The first step in the bootstrap is to obtain a conservative field by taking the modulus of the finite difference gradient vector; this is a numerical approximation of an (isotropic) differentiation of order 1. As long as  $H < 1$ , the double trace moment technique applied to the resulting field will give reasonable estimates of  $\alpha$ ,  $C_1$  [see Lavallée *et al.* (1993) for details, numerical simulations and tests; see also Schertzer *et al.* (1997) for more discussion]. The main drawback is that the scaling is somewhat broken by the finite difference approximation to the gradient, as well as when the absolute value of the latter is taken. [Veneziano & Iacobellis (1999) has complained that—as pointed out in Lavallée *et al.* (1993)—this operation can break the scaling over a range of factor 2–4 or so in scale at the extreme smaller scales. However, if the scaling is over a wide enough range, this problem is not too important since the larger scales can be used to obtain accurate exponent estimates without directly using the extreme small scales.] This method (applied to both the higher- and lower-wavenumber regimes) yielded  $\alpha \approx 1.9$  and  $C_1 \approx 0.1$ . To obtain the refined estimates we use these values to estimate  $H$ , which can then be used to differentiate the field fractionally. This is done by comparing the observed

spectral exponents ( $\beta$ ) with those of the conserved process given by (Monin & Yaglom 1975),

$$\beta_{\text{con}} = 1 - K(2). \quad (8)$$

This relation for the spectral exponent of a conservative multifractal cascade can be understood from the fact that the power spectrum is the Fourier transform of the autocorrelation function, which is a second-order moment. The value of  $H$  is then estimated from

$$H = \frac{\beta - \beta_{\text{con}}}{2} \quad (9)$$

(the factor of 2 comes from the fact that the energy density is the integral of the square of the Fourier modulus).

Our revised analyses of the high- and low-wavenumber parts of the data give  $\alpha = 1.92 \pm 0.03$  for the higher- and  $\alpha = 2.0 \pm 0.1$  for lower-wavenumber parts of the data. Since the DTM is mostly sensitive to the behaviour of the moments near  $q=0$ , a value  $\alpha=2$  directly implies no more than the analyticity of  $K(q)$  at the origin, that is, a Taylor series expansion of  $K(q)$  about  $q=0$  may have higher-order terms. Indeed, it is only in the case of the universal ‘log-normal’ multifractal that there are only quadratic terms. Note that the lower-wavenumber region of the data corresponds to the ‘intermediate’ range discussed in Paper I [that is, between the Curie wavenumber and approximately  $(2000 \text{ km})^{-1}$ ]. The values obtained for  $C_1$  differed for the higher- and lower-wavenumber ends of the spectrum. The estimate for the high-wavenumber regime for  $C_1$  is  $0.14 \pm 0.01$ ; the estimate for the intermediate- (lower-) wavenumber regime is  $C_1$  (see Table 1 for a full intercomparison of parameter estimates). Since the DTM (Figs 2a and b) is mostly sensitive to the low- $q$  behaviour, the fall-off in the ratio of high- and low-wavenumber  $K(q)$  (Fig. 3) shows that either  $\alpha$  is substantially different for the two regimes or more likely that universal multifractals are only low- $q$  approximations to the statistics; see discussion below and the simulation (universal multifractals may, however, still be a good model for  $\mathbf{M}$ ). We also note that values obtained from the  $K(q)$  (Fig. 3) graph for the multifractal parameters are for the most part in good agreement with those obtained from the DTM; however, as the  $K(q)$  fit is non-linear and the range of scales over each wavenumber end is limited, we use the values obtained from the DTM.

Fig. 1 shows the scaling of various moments of the high-wavenumber part of the data. Figs 2 (a) and (b) show the fits of the DTM. We note that these estimates are performed over a limited range of scales and are thus not as precise as

those taken over a larger scaling range. Note that the value of  $\alpha$  (corresponding to an order of non-analyticity at  $q=0$ ) is somewhat smaller than, but close to, the value 2 [corresponding to analytic  $K(q)$  and—at least approximately—log-normal statistics].

Strictly speaking, the scaling exponents are determined from an ensemble average. It is necessary to have a large number of independent measurements of the field because of intermittency and the extreme variability of multifractal fields. Certain orders of singularity, corresponding to very high field values, may in fact have a co-dimension larger than the dimension of space and will almost certainly not appear in any given realization/example of the field. Nevertheless, these values will appear in a sufficiently large number of realizations and can be statistically important, dominating the statistical moments of high enough order. They will in general cause a divergence of the high-order moments of the field (Schertzer & Lovejoy 1985, 1987), associated with a non-classical form of self-organized criticality (Schertzer & Lovejoy 1994), for magnetism; this will be discussed elsewhere.

#### 4 DEDUCING THE $q$ TH-ORDER $\mathbf{M}$ STATISTICS FROM THE SURFACE $\mathbf{B}$ SURVEYS

In Paper I we showed how to relate the surface  $\mathbf{B}$  to the volume distribution of  $\mathbf{M}$ . Since scaling non-linear geophysical processes are expected to be multifractal, *a priori* we will assume that  $\mathbf{M}$  is multifractal. In addition, since the surface  $\mathbf{B}$  field is linearly related to the source  $\mathbf{M}$  field, if the latter is multifractal, then we expect that—at least over certain ranges—the former will also be multifractal. Unfortunately, the multifractal problem of how to relate the statistics of the two fields to all orders is much more difficult than the relatively straightforward second-order problem; we will rely on explicit multifractal models. For several reasons, the best place to begin modelling is with the  $\mathbf{M}$  rather than surface  $\mathbf{B}$  field. This is likely to be simpler since we have seen that due to anisotropy and Curie depth effects, we may expect there to exist several regimes for the  $\mathbf{B}$  field, even if there is only one for the  $\mathbf{M}$  field. In addition, while the inverse problem (determining the 3-D  $\mathbf{M}$  given the surface  $\mathbf{B}$ ) is not uniquely determined, the determination of  $\mathbf{B}$  from  $\mathbf{M}$  is unique. Finally, the non-linear processes responsible for the magnetization distribution are plausibly universal multifractals, whereas the surface  $\mathbf{B}$  field is linearly derived from  $\mathbf{M}$  (and therefore is unlikely to be universal).

**Table 1.** Intercomparison of the conservative multifractal parameters  $C_1$ ,  $\alpha$  for surface  $\mathbf{B}$  field and simulated  $\mathbf{M}$ . The terms ‘high’ and ‘intermediate’ refer to the wavenumber regime immediately above and below the Curie wavenumber, respectively. The ‘non-linear’ estimates were for the entire  $K(q)$  function for  $q < 3$ , whereas the DTM is more sensitive to the range  $q$  near 0. No errors are quoted for the simulated  $\mathbf{M}$  since these were the input parameters used in the model. The vertical value of  $C_1$  is the horizontal value divided by  $H_z = 1.7$  for the simulation. The  $H$ -values were not given because they depend almost entirely on  $\beta$  since  $C_1$  is small (see eqs 8 and 9). Using the values  $\beta_h = 2$ ,  $\beta_i = \beta_h - 1 = 1$  from Paper I, we obtain  $H_{Bh} = 0.61$ ,  $H_{Bi} = H_{Bh} - 0.5 = 0.11$ ;  $H_M = 0.2$  (see text). For comparison, the quasi-Gaussian monofractal has  $C_1 = 0$ , whereas the ‘ $\beta$  model’ monofractal has  $\alpha = 0$ ,  $H = 0$ .

	Empirical B DTM (high regime)	non-linear (high)	DTM (intermediate)	non-linear (intermediate)	Simulated B DTM (high)	DTM (intermediate)	Simulated M horizontal	vertical
$C_1$	$0.14 \pm 0.01$	$0.14 \pm 0.01$	$0.08 \pm 0.01$	$0.09 \pm 0.01$	$0.16 \pm 0.06$	$0.09 \pm 0.02$	0.08	0.047
$\alpha$	$1.92 \pm 0.03$	$1.87 \pm 0.05$	$2.0 \pm 0.10$	$2.2 \pm 0.2$	$1.8 \pm 0.10$	$2.05 \pm 0.09$	1.98	1.98

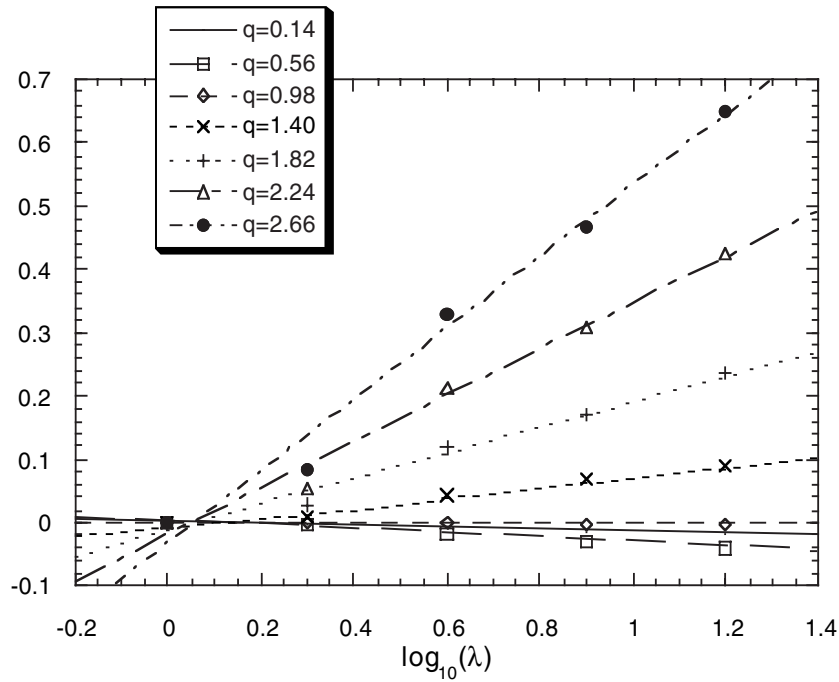


Figure 1. Scaling of the moments of the high-wavenumber end of the fields ( $\lambda=1$  corresponds to  $812.8 \times 2^4 \approx 12$  km).

To infer the statistics of  $\mathbf{M}$ , we start with the observation (Appendix A, Paper I) that for the relevant spectral (second-order) exponents, the surface  $\mathbf{B}$  spectral densities are the same as the power-law filtered vertical integral of the  $\mathbf{M}$  spectral density. Since this filter only changes the values of the fractional integration  $H$ , this predicts that  $K_h(2) \approx K_i(2) = K_M(2)$  (where the subscripts  $h$  and  $i$  refer to the high- and intermediate-regime wavenumber surface  $\mathbf{B}$  statistics), which is approximately empirically verified (Fig. 3). [The term ‘intermediate’ refers to the regime  $k_{ic} < K < k_c$  with  $k_{ic} \approx (2000 \text{ km})^{-1}$ ; see Paper I. Of course, for the data sets here whose lowest wavenumbers are  $(200 \text{ km})^{-1}$ , the intermediate regime corresponds to the lowest empirically accessible wavenumbers.] However, we have seen empirically that in the low- $q$  limit (as characterized by the DTM, which is mostly sensitive to  $q < 1$  statistics), the ratio  $K_h(0)/K_i(0) \approx 2$ , which is roughly the same value as that of  $H_z$  obtained by fitting the empirical and theoretical spectra (Paper I). Numerical simulations (described below) confirm this connection. In addition, the relation  $K_h(0)/K_i(0) = H_z$  would result if for weak intensity fluctuations (corresponding to low-order singularities  $\gamma$ , or equivalently low-order moments  $q \approx 0$ ) the horizontal anomaly wavenumber  $K$  and the vertical magnetization structures at wavenumber  $k_z$  are roughly related in a one-to-one way as follows:

$$K \approx k_z^{H_z}. \quad (10)$$

Using this relation between  $K$ ,  $k_z$ , we can see that a given factor of  $\lambda$  in scale in the vertical corresponds to an equivalent horizontal factor  $\lambda_i$  in the intermediate-wavenumber regime, whereas it corresponds to  $\lambda_h^{H_z}$  in the high-wavenumber regime, that is, for low enough  $q$  we would have

$$\lambda_i = \lambda_h^{H_z}. \quad (11)$$

If we now assume that this relation holds for low enough order statistics using  $\langle \varepsilon_q^\lambda \rangle \approx \lambda^{K(q)}$ , we have

$$\frac{K_h(0)}{K_i(0)} = H_z, \quad (12)$$

as observed in Fig. 2. As a first approximation, it is therefore possible to use large  $q$  statistics of  $\mathbf{B}$  [i.e. where  $K_h(q)$  and  $K_i(q)$  are roughly equal] as a proxy for a conservative cascade contribution to the  $\mathbf{M}$  statistics. The numerics show that we can in fact do a little better than this since they show that for the low-wavenumber  $\mathbf{B}$  regime, we have  $K_i(q) \approx K_M(q)$  for all  $q$ ; we therefore use  $K_i(q)$  to deduce the  $K_M(q)$ , i.e. we take  $C_1 = 0.08$ ,  $\alpha = 1.98$ . The only remaining parameter to determine is  $H_M$ , the non-conservation parameter for the horizontal magnetization multifractal.  $H_M$  can be determined using the fact that  $s = \beta_h + 2 = \beta_{x,M} + H_z + 1$  and  $\beta_{x,M} = 1 - K_M(2) + 2H_M$  (see eqs 8 and 9). We thus obtain the estimate

$$H_M = \frac{1}{2} (\beta_h + K_M(2) - H_z). \quad (13)$$

Using the values  $s = 4$  (hence  $\beta_h = 2$ ),  $K_M(2) = K_i(2) \approx 0.16$  (from Fig. 3) and  $H_z = 1.7$ , we find  $H_M = 0.2$  (note that these values are all approximate). In this way, the observed  $\mathbf{B}$  field gives us the statistical information necessary to make a multifractal simulation of the  $\mathbf{M}$  field, and hence to model the  $\mathbf{B}$  field. The various assumptions are thus checked by numerical simulation. We turn to this in the next section.

## 5 ANISOTROPIC SIMULATIONS OF $\mathbf{B}$ AND $\mathbf{M}$

We have seen that although we were able to obtain an exact spectral relation between  $\mathbf{M}$  and  $\mathbf{B}$ , the relationship between the full statistics of  $\mathbf{B}$  and  $\mathbf{M}$  was not so easy to calculate

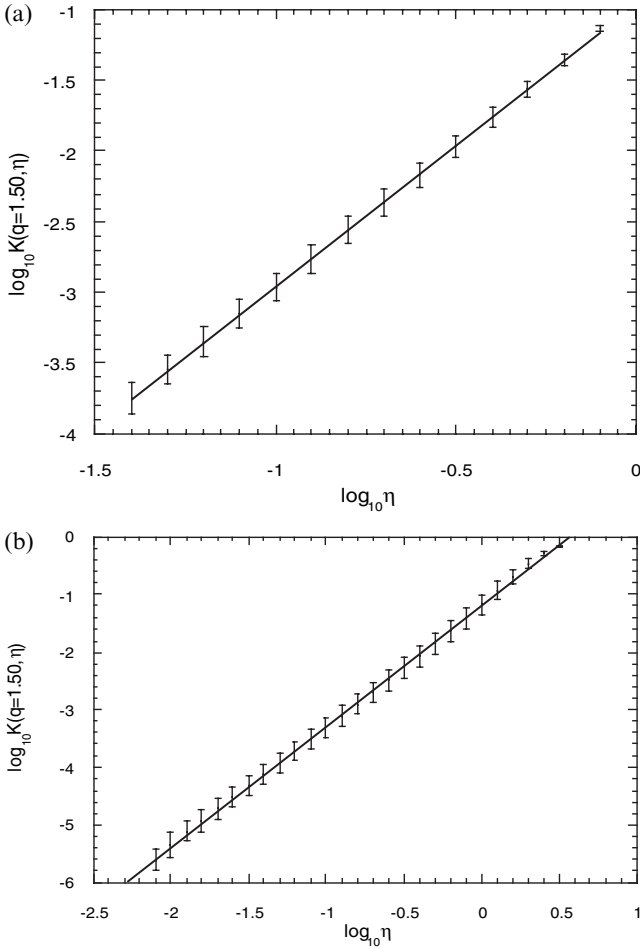


**Figure 2.** (a) The exponent  $K(q, \eta)$  as a function of  $\eta$  for  $q=1.5$  obtained as slopes of curves such as those in Fig. 1 (high-wavenumber end of the data sets). The fit gives the values  $\alpha=1.92 \pm 0.03$  and  $C_1=0.14 \pm 0.01$ . (b) The exponent  $K(q, \eta)$  as a function of  $\eta$  for  $q=1.5$  obtained as slopes of curves such as those in Fig. 1 for the low-wavenumber end of the data sets, corresponding to the intermediate range discussed in Paper I. The fit gives the values  $\alpha=1.98 \pm 0.10$  and  $C_1=0.08 \pm 0.01$ .

theoretically. In the previous section we saw that a kind of a ‘bootstrap’ can be used in which, with the help of the data and some theoretical arguments, an intelligent guess of the  $\mathbf{M}$  statistics is made; the latter is then used to simulate  $\mathbf{M}$  and hence  $\mathbf{B}$ . Let us quickly review this in a little more detail and describe the multifractal numerical simulation procedure. As a first step in determining the statistics of  $\mathbf{M}$  we have used the fact that it should respect the anisotropic scaling symmetry. Such an anisotropic field of  $\mathbf{M}$  (assumed throughout to be parallel to the  $z$ -axis) respects the following:

$$|\Delta \mathbf{M}|_\lambda = |\mathbf{M}(\mathbf{x} + T_\lambda \Delta \mathbf{x}_1) - \mathbf{M}(\mathbf{x})| = (T_\lambda \chi_1) \lambda^{-H} = \chi_\lambda \lambda^{-H}, \quad (14)$$

where  $\Delta \mathbf{x}_1$  is a unit separation vector (i.e. it lies on the unit ball),  $\chi$  is the conserved flux of the cascade producing the magnetization,  $\chi_1$  is the flux averaged over a unit ball and  $T_\lambda \chi_1 = \chi_\lambda$  is the flux averaged over a ball  $B_\lambda = T_\lambda B_1$ , where  $T_\lambda = \lambda^{-G}$ . For reference, note that if  $\chi_\lambda$  is replaced by a Gaussian white noise,  $K_M(q)=0$  and  $M$  will be a (monofractal) fractional Brownian motion, and that the quite different monofractal ‘ $\beta$  model’ has  $\alpha=0$ ,  $C_1 > 0$ ,  $H=0$ .

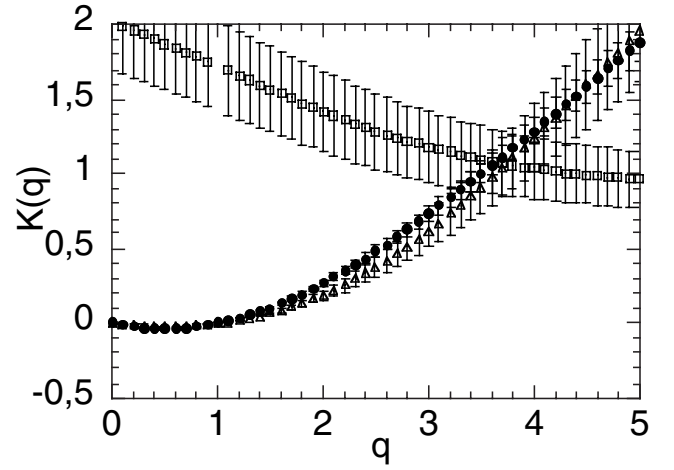


**Figure 3.** Exponent  $K(q)$  from the trace moments of the higher- and lower-wavenumber parts of the data sets. The fit to the moment scaling function,  $K(q)$ , gives the values  $\alpha=1.87 \pm 0.05$  and  $C_1=0.14 \pm 0.01$  (for the higher end circles) and  $\alpha=2.2 \pm 0.2$  and  $C_1=0.09 \pm 0.01$  (for the lower end triangles). These values are within the uncertainty of the values found from the DTM, with the exception of  $\alpha$  for the low-wavenumber part, which is marginally outside. The graph also shows the ratio between high- and low-wavenumber  $K(q)$ , indicating that it has some  $q$  dependence and a value of  $\sim 1.0$ – $2.0$  (squares).

The conserved flux is required to satisfy

$$\langle \chi_\lambda^q \rangle = \lambda^{K_M(q)}, \quad (15a)$$

with scale-by-scale conservation implying  $\langle \chi_\lambda \rangle = \text{constant}$  (independent of scale) so that  $K_M(1)=0$ . Note that taking ensemble averages of  $q$ th powers of eq. (14) coupled with eq. (15a) yields the structure function

$$\langle |\Delta \mathbf{M}|_\lambda^q \rangle = \lambda^{-\xi_M(q)} \quad (15b)$$

with exponent

$$\xi_M(q) = qH_M - K_M(q). \quad (15c)$$

The use of the generator

$$\mathbf{G} = \begin{pmatrix} 1 & 0 & 0 \\ 0 & 1 & 0 \\ 0 & 0 & H_z \end{pmatrix}$$

implies that the 1-D horizontal ( $x$ ) and vertical ( $z$ ) statistics are the same if the scale ratio  $\lambda$  is replaced by  $\lambda^{H_z}$ . Hence, writing  $K_{x,M}(q)$  for the 1-D horizontal exponent,  $K_{z,M}(q)$  for the 1-D vertical exponent, we find that the two are related to the full anisotropic scaling exponent  $K_M(q)$  as follows:

$$K_M(q) = K_{x,M}(q) = H_z K_{z,M}(q). \quad (16a)$$

Similarly, from eq. (14),

$$H_M = H_{x,M} = H_z H_{z,M}. \quad (16b)$$

Hence, for structure functions we obtain

$$\xi_M(q) = \xi_{x,M}(q) = H_z \xi_{z,M}(q). \quad (16c)$$

These relations ensure that the magnetization spectral exponents respect the relation  $(\beta_x - 1) = H_z(\beta_z - 1)$ .

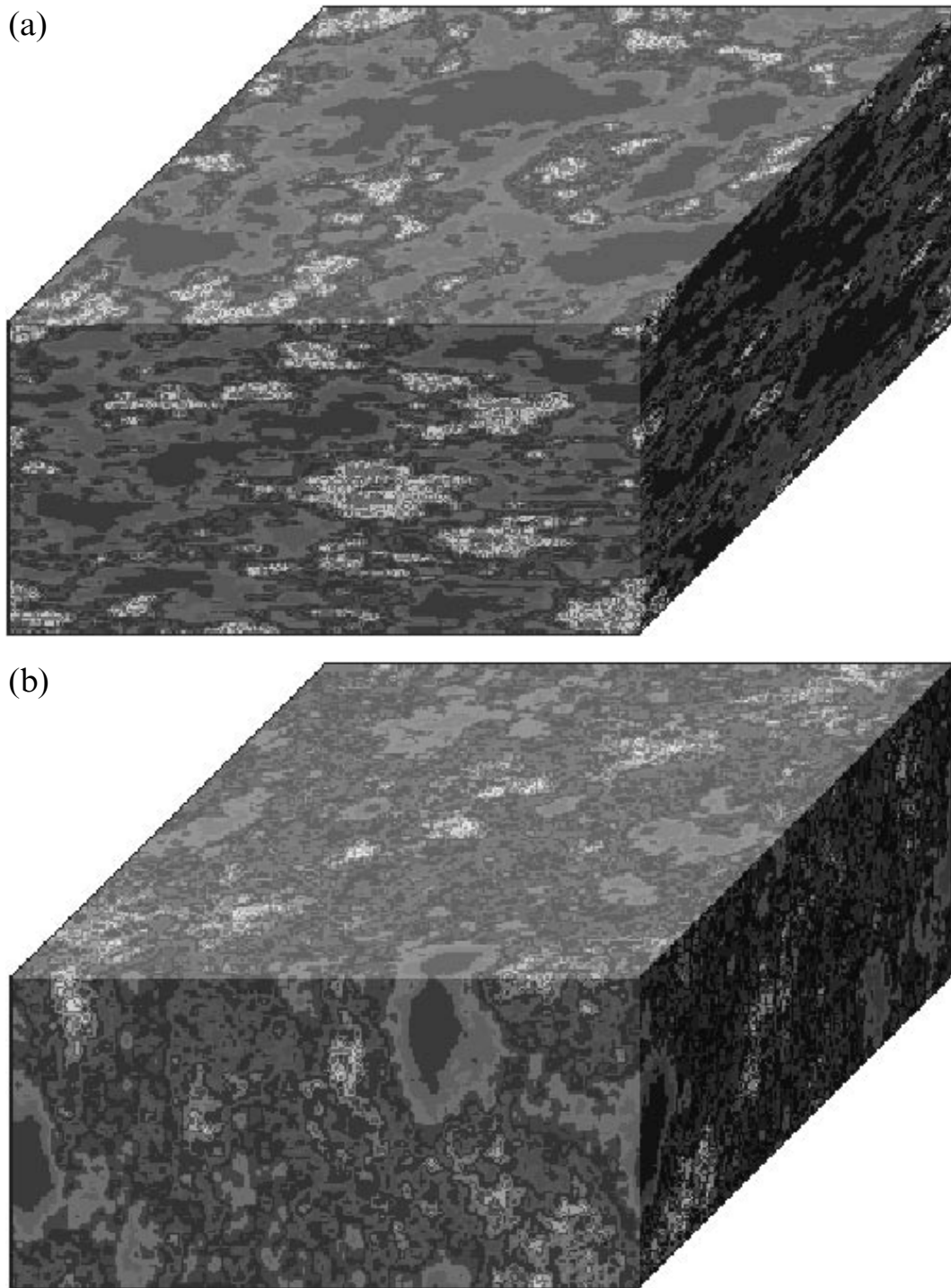


**Figure 4.** (a) Numerical multifractal simulation of the  $\mathbf{M}$  field with  $\alpha=1.98$ ,  $C_1=0.08$ ,  $H_M=0.2$ ,  $H_z=1.7$  (implying  $s=4$ ) on a  $128 \times 128 \times 64$  pixel grid with the spheroscale = 128 pixels. Because of the large dynamical range variability, the colour scale is chosen on a log  $\mathbf{M}$  scale here and in all the displays below. Notice that structures are flatter and flatter at smaller scales. This is not a realistic model for  $\mathbf{M}$  because the thickness of this simulation (half the spheroscale) is far larger than the Curie depth cut-off. The direction of  $\mathbf{M}$  is assumed here and below to be fixed in the  $z$ -direction. (b) Numerical multifractal simulation of the  $\mathbf{M}$  field with  $\alpha=1.98$ ,  $C_1=0.08$ ,  $H_M=0.2$ ,  $H_z=1.7$  (implying  $s=4$ ) on a  $128 \times 128 \times 64$  pixel grid with the spheroscale = 1 pixels. Notice that structures are more and more vertically oriented at larger scales and roughly spherical at small scales. Although the  $\mathbf{M}$  spheroscale is apparently empirically of the order of the size of the earth, so that these very large scales are not realistic for  $\mathbf{M}$ , this simulation could be a qualitatively correct simulation for mantle rock density where the spheroscale is plausibly of the order of 100 km. In that case, the vertically aligned structures would correspond to convective cells and ‘hotspots’. The direction of  $\mathbf{M}$  is assumed here and below to be fixed in the  $z$ -direction. Figs 4, 5, 7, 10, 11, 12 and 13 may be viewed in colour in the online version of the journal (<http://www.blackwell-synergy.com>).

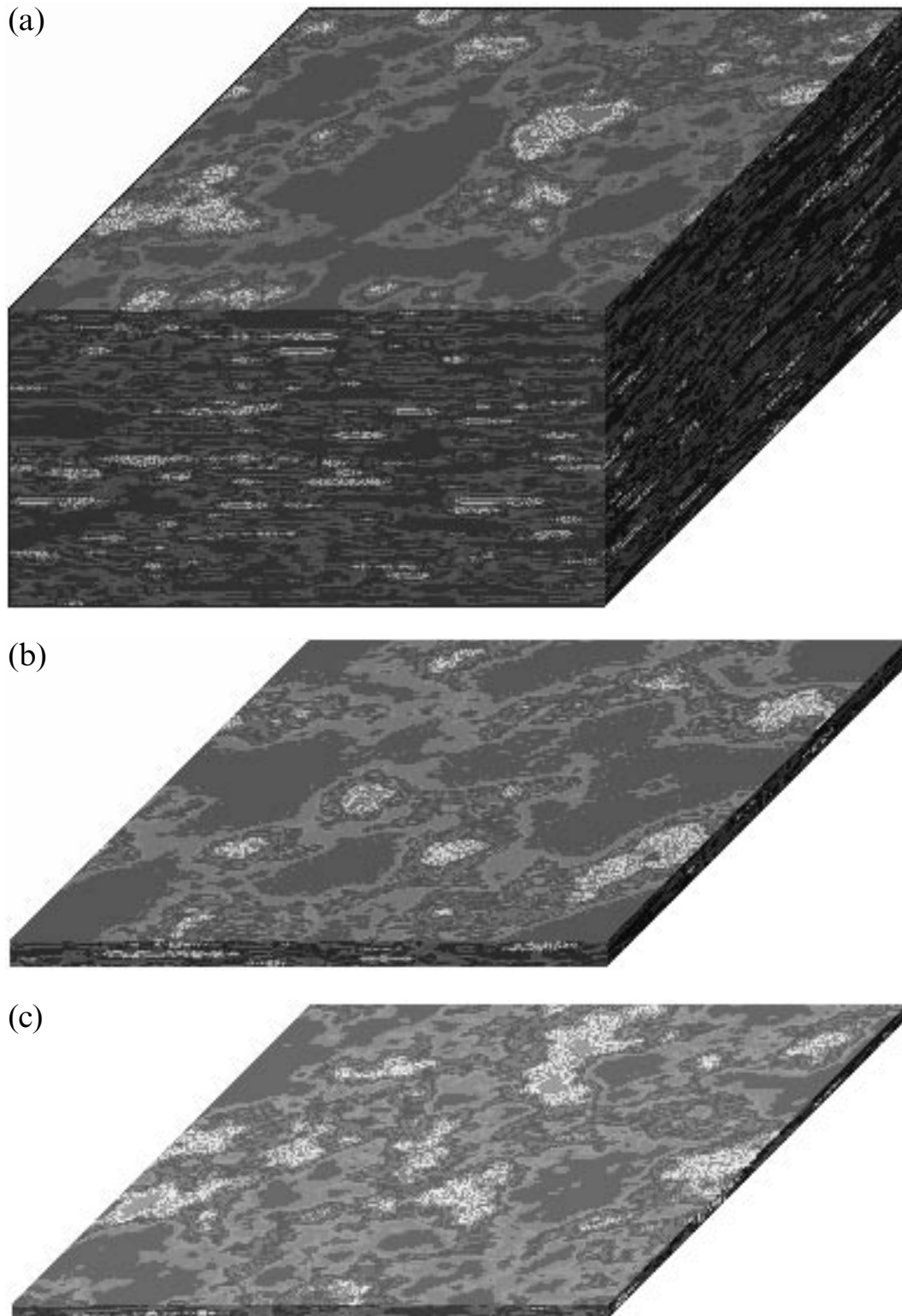


**Figure 5.** (a) Simulated  $\mathbf{M}$  field for horizontally isotropic crustal magnetization. The vertical anisotropy has  $H_z=1.7$ , and  $s=4$ ,  $H=0.2$ ,  $\alpha=1.98$ ,  $C_1=0.08$ . The spheroscale was taken to be only  $\sim 2500$  km; the simulation is a region  $32 \times 32 \times 16$  km; the resolution is 0.25 km. This is a reasonably realistic crustal section, although the spheroscale was taken to be a bit too small in order that strata may be easily visible. (b) Simulated  $\mathbf{M}$  field for horizontally isotropic crustal magnetization; same parameters as (a). The simulation is  $128 \times 128 \times 32$  km; the resolution is 1 km and only the portion above the Curie depth of 10 km is shown. (c) Simulated  $\mathbf{M}$  field for horizontally isotropic crustal magnetization; same parameters as (a). The simulation is  $512 \times 512 \times 16$  km; the resolution is 4 km. (d) Simulated  $\mathbf{M}$  field for horizontally isotropic crustal magnetization. The vertical anisotropy has  $H_z=1.7$ , with a spheroscale of  $\sim 2500$  km (also  $s=4$ ,  $H=0.2$ ,  $\alpha=1.98$ ,  $C_1=0.08$ ). The simulation is  $4 \times 4 \times 16$  km; the resolution is 62.5 m. The cut-out shows the stratification and the presence of anomalies at all depths.

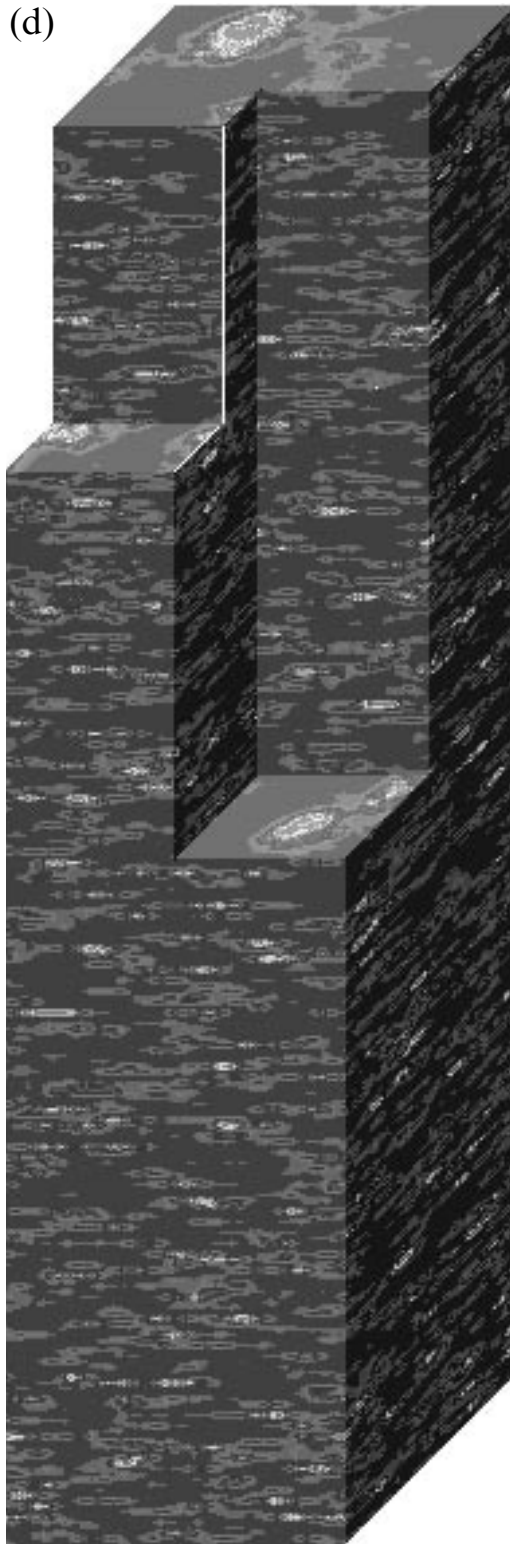
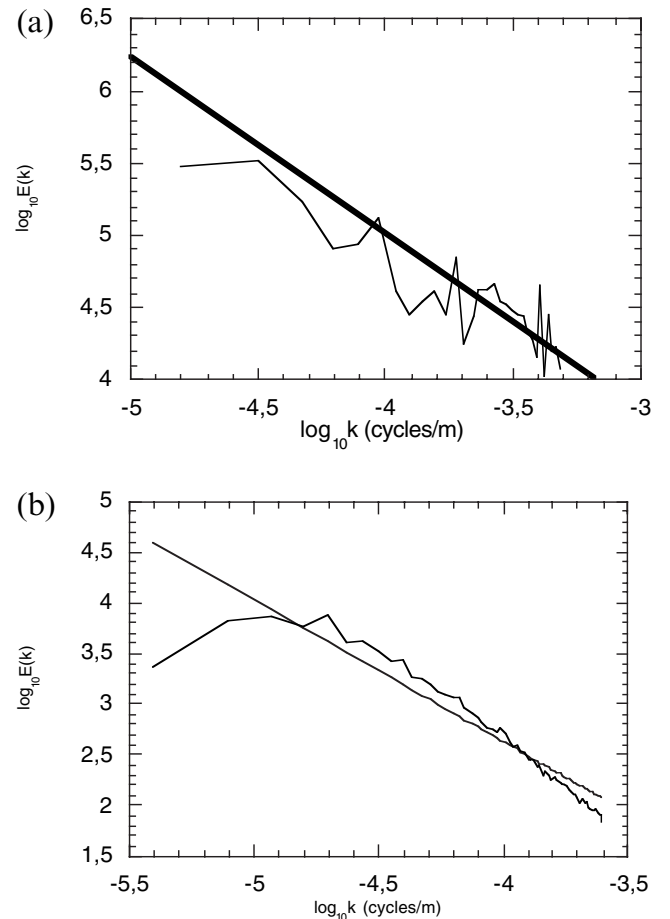


Figure 5. (Continued.)

The final step is to use the approximation discussed in the previous subsection viz. that the intermediate wavenumber  $\mathbf{B}$  statistics should be the same as the horizontal  $\mathbf{M}$  statistics:  $K_i(q) \approx K_{x,M}(q) = K_M(q)$ . The multifractal parameters used to simulate the magnetization were therefore  $\alpha = 1.98$ ,  $C_1 = 0.08$ ; in addition, using  $s = 4$ ,  $H_z = 1.7$ , we obtained  $H_M = 0.2$ .

The numerical details of the multifractal simulation procedure for  $\mathbf{M}$  are given in Pecknold *et al.* (1993) (see also Wilson *et al.* 1991 and Marsan *et al.* 1996 for extensions to space–time modelling). In brief, the process starts with a subgenerator,  $\gamma_g$ , which is an uncorrelated Gaussian or Levy noise (with the desired Levy parameter  $\alpha$ ; the amplitude of the Levy fluctuations of the subgenerator determines  $C_1$ ). This subgenerator is then fractionally integrated (power-law filtered) to yield an exactly  $1/f$  generator  $\Gamma_\lambda$ ; the latter is exponentiated to yield the conservative multifractal  $\chi_\lambda = e^{\Gamma_\lambda}$ . Finally,  $\chi_\lambda$  is power-law filtered (exponent  $H_M$ ) to yield  $\mathbf{M}$ . For a self-similar process, all the fractional integrals are isotropic, whereas in the anisotropic version, all isotropic fractional integrals are replaced by the corresponding anisotropic ones. This means, for example, that the fractional integral order  $H$ , which in the self-similar version is a power-law filter (Fourier space multiplication) of  $|\mathbf{k}|^{-H}$  (i.e. with the usual vector modulus), is replaced in the anisotropic versions by the scale function (defined by  $\mathbf{G}$ ; see Paper I, Section 3) so that the filter involves Fourier space multiplication by  $\|\mathbf{k}\|^{-H}$ . Note that the simulations below were generally performed on a total of  $2^{20}$  gridpoints on a personal computer.



**Figure 6.** (a) 1-D Power spectra  $E(k_z)$  for borehole  $\mathbf{M}$  for simulated fields  $128 \times 128 \times 32$  pixels, each pixel = 1 km; same parameters as Fig. 5(b) but with spheroscale = 5000 km. Due to the Nyquist wavenumber the vertical spectrum can only be calculated over a range of factor 16 in scale. The straight line shows the theoretical slope  $\beta_z = 1.17$ . (b) Horizontal power spectra  $E(K)$  for  $\mathbf{M}$  for seven simulated fields, same parameters as Fig. 6(a). The straight line shows the theoretical slope  $\beta_x = 1.3$ .

Before considering more realistic stratification parameters, let us first consider the effect of variable spheroscale in the vertical plane. Figs 4(a) and (b) visually display the way the typical structure shapes change with scale. Fig. 4(a) shows the effect of stratification decreasing at larger and larger scales, while Fig. 4(b) shows how it can reverse and yield vertically aligned structures at scales even larger than the spheroscale. Although in Paper I we found that the data suggest that the  $\mathbf{M}$  spheroscale is too large for this scale range to be physically realized for the planetary  $\mathbf{M}$  field, since the spheroscale for rock density

is much smaller [apparently of the order of 100 km, although with comparable  $H_z$  values; see Lovejoy *et al.* (2001b)], Fig. 4(b) may therefore represent a section of the mantle several thousand kilometres across with the vertically aligned structures corresponding to ‘convective cells’. Fig. 5 shows a fairly realistic set of parameters at varying scales with respect to the Curie depth and varying model resolutions. All structures/anomalies are random singularities of various orders, and are produced naturally by the multifractal process; they do not need to be introduced by hand. Note that the same basic

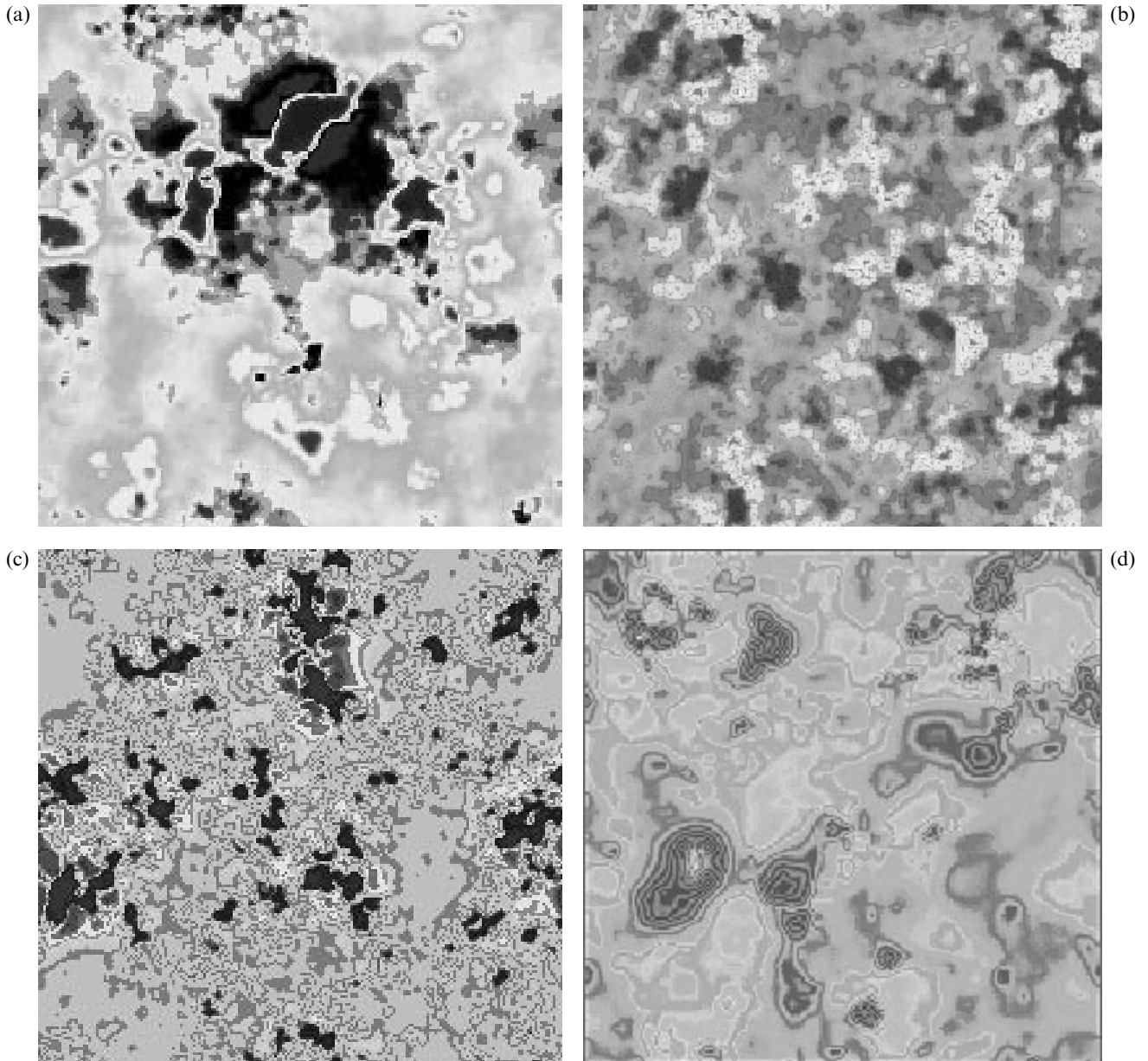


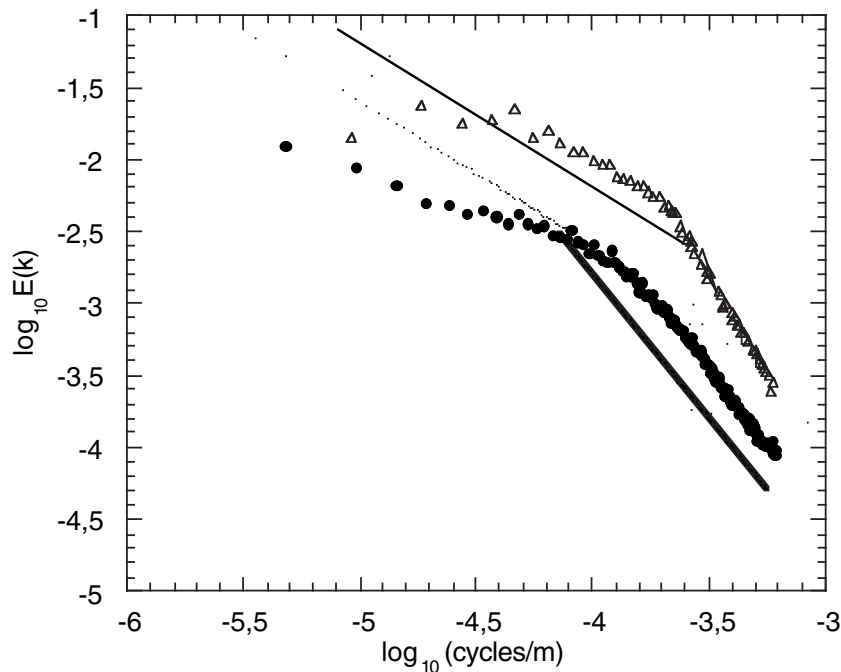
**Figure 7.** (a) Surface  $\mathbf{B}$  field from simulation shown in Fig. 5(a), i.e. with  $128 \times 128 \times 64$  pixels, each pixel = 0.25 km (the entire simulation represents a region 32 km across). The Curie depth = 16 km so that nearly the entire field shown is in the smooth, high-wavenumber regime  $\beta_h = 2$ . (b) The surface  $\mathbf{B}$  field resulting from the simulated crustal  $\mathbf{M}$  field in Fig. 5(b). Since the entire region simulated is 128 km across and the Curie depth is 10 km, the transition from high- to intermediate-wavenumber regime is in the middle of the range shown; the high-wavenumber structures are noticeably smoother than the lower ones. (c) Surface  $\mathbf{B}$  field from simulation Fig. 5(c) with  $128 \times 128 \times 4$  pixels, each pixel = 4 km (the entire simulation represents a region 512 km across). The Curie depth = 16 km so that most of the field shown with the exception of the very highest wavenumbers is in the (rough) intermediate-wavenumber regime with  $\beta_i = 1$ . (d) Surface  $\mathbf{B}$  field from the simulation in Fig. 5(d),  $64 \times 64 \times 256$  pixels, each pixel = 62.5 m (the entire simulation represents a region 4 km across). The Curie depth = 16 km so that the entire field shown is in the smooth high-wavenumber regime with  $\beta_h = 2$ .

geometries of structures will occur if  $k_s, H_z$  are fixed but  $\alpha, C_1, H_M$  are varied. Of the latter, increasing (decreasing)  $H_M$  will make all structures more and more smooth (rough), whereas increasing (decreasing)  $C_1$  will cause the simulation to be increasingly (decreasingly) dominated by one or two very violent anomalies. A high value of  $\alpha$  will make this change happen more quickly for a given change in  $C_1$ .

Before comparing the statistics of the simulated surface  $\mathbf{B}$  field with those of the data, we checked the numerical accuracy of the  $\mathbf{M}$  simulation by calculating the ensemble average spectrum of seven simulations (the same number as the number of  $\mathbf{B}$  surveys) in both the horizontal and vertical directions (Figs 6a and b). The theoretical lines (slopes calculated from eqs 20a and b in Paper I) are shown for reference; the agreement was judged reasonable, although there seemed to be a slight underestimate at the very lowest (factor of two) horizontal wavenumbers, and also the highest factor of two. Such ‘finite size’ numerical effects near the extreme ends of the range of the model were difficult to avoid and are common in this type of simulation. The vertical spectrum was quite close to the theoretical slope, although again with a slight underestimate of the variability at the lowest factor of two in wavenumber. Note that the realization-to-realization variability about the theoretical power laws is quite large; this is because in multifractals the spectral exponents on individual realizations are random variables with large variability (see Lovejoy *et al.* 2001c for the related problem of conditional spectra). This explains why the empirical susceptibility data (magnetization surrogates) analysed in Paper I gave such poor estimates of the exponents. Note that in order to show the scaling of the simulation over more than one order of magnitude, the borehole spectrum is over the entire size of the field and neglects the presence of the Curie depth. Also note that the values for  $E(K), E(k_z)$  appear to be roughly compatible with a very large spheroscale.

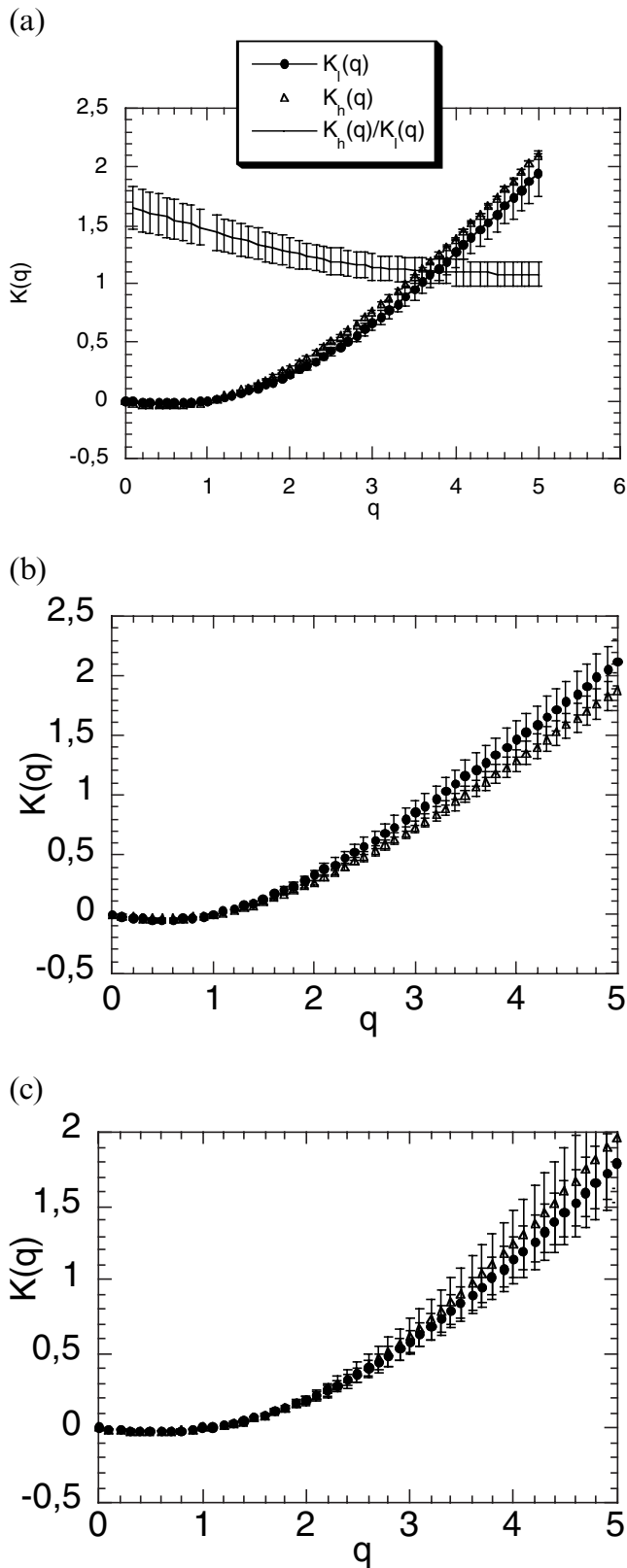
We can now calculate the horizontal  $\mathbf{B}$  fields corresponding to the  $\mathbf{M}$  fields in Figs 5(a)–(d); this was done using eq. (6) of Paper I (Figs 7a–d). The corresponding spectrum of the simulation that best straddles the transition region (Fig. 5b) is shown in Fig. 8. In order to obtain the same overall variability as the seven empirical data sets, a total of seven such simulations were performed. Except for the extreme low-wavenumber factor of 2–3 (presumably inherited from the finite size effects of the  $\mathbf{M}$  simulation), this reproduces the theoretical spectrum as expected. Fig. 8 shows that the simulated aeromagnetic field spectrum shows roughly the same spectral scaling behaviour as the empirical fields (including the break, shown for comparison) and indicates good correspondence of the model with the data. The weakest agreement is in the transition zone (near  $K \approx k_c$ ); this is likely to be the result of the unrealistic treatment of the Curie depth as being simply an abrupt spectral cut-off, whereas in fact it is presumably a spatially irregular (fractal) real-space cut-off.

Fig. 9(a) shows the simulated field moment scaling function  $K(q)$  for both high and low wavenumbers and fits to these, along with the ratio of  $K_h(q)$  to  $K_i(q)$  (again for seven realizations). In order to improve the estimates we have performed separate simulations for the high- and low-wavenumber regimes, that is, we changed pixel size so that the largest and then the smallest horizontal scales, respectively, corresponded to the Curie depth (Figs 7b and c show the typical  $\mathbf{B}$  field realizations used here). This gave us the maximum possible range of scales (factors of 128) with which to estimate the scaling exponents. Perhaps the most important point is that although the error bars are not as small as we would like, the ratio of  $K_h(q)$  to  $K_i(q)$  does decrease from a value of  $\approx H_z (= 1.7$  in the simulations) to  $\approx 1$  as we go from  $q \approx 0$  to  $q > 1$  (the variation is much the same as in the data, *cf.* Figs 3 and 9b and c); this provides *a posteriori* justification for the use of the multifractal



**Figure 8.** Power spectrum of simulated aeromagnetic fields (triangles) superimposed on the power spectrum for the data (circles). The theory and data each involve averaging over seven realizations. The straight lines are the high- and intermediate-wavenumber theoretical slopes,  $\beta_h = 2, \beta_i = 1$ . The vertical scales are arbitrary and the two curves are somewhat offset for clarity.

parameters determined from the low-wavenumber regime of **B**. Figs 9(b) and (c) compare the moment scaling functions of the simulated fields to those of the data. We note that both  $K_h(q)$  and  $K_i(q)$  for the simulation are very close to those from the



data, thus at all scales ( $K$ ,  $\lambda$ ) and at all intensities ( $\gamma$ ,  $q$ ) our model is in good agreement with those of the data; Table 1 shows a detailed intercomparison. Note that for moments greater than  $q \approx 3$ , all the  $K(q)$  functions become roughly linear; this is a multifractal phase transition and indicates that the sample size is too small to estimate the corresponding moments and  $K(q)$  accurately; the values are dominated by single large gradients and the data/simulation comparisons are no longer expected to be very good (Schertzer & Lovejoy 1992, 1994). Overall, this good agreement gives excellent vindication of the ‘bootstrap’ method used to deduce the **M** statistics from the surface **B** statistics.

## 6 ANALYSIS AND SIMULATION OF HORIZONTAL SCALING ANISOTROPIES

### 6.1 GSI analysis of the fields

Up until now, we have concentrated our attention on the vertical/horizontal anisotropy/stratification, assuming—for simplicity—horizontal isotropy/self-similarity. However, shears and tectonic and other (presumably scale-invariant) processes lead to horizontal stretching rotation and more general transformations of structures with scale; in this section we characterize the resulting horizontal anisotropy and show how to model it. Although unsurprisingly the overall magnitudes of the horizontal anisotropies turn out to be much smaller than those of the vertical, they nevertheless characterize the morphology/texture of the **M** and **B** fields. A fully realistic treatment of the anisotropy would recognize that the anisotropy is not only scale-dependent but also position-dependent; it would require the use of a non-linear generalized scale invariant with a stochastic generator. Practical ways of handling such general scale changes are still in the experimental stage (see Addor *et al.* 2000); we therefore approximated the anisotropy using a linear GSI approximation in which the generator is a matrix.

**Figure 9.** (a) Exponents  $K_h(q)$ ,  $K_i(q)$  determined from the trace moments of the high- and intermediate-wavenumber parts of the simulated **B** field with parameters  $H_z=1.7$ ,  $s=4$ ,  $H=0.2$  the same as in Figs 5 and 7 (implying  $\beta_{xM}=1.3$ ,  $\beta_{zM}=1.17$ ,  $\beta_1=1$ ,  $\beta_h=2$ ). The fit to the moment scaling function,  $K(q)$ , gives the values  $\alpha=1.8 \pm 0.1$  and  $C_1=0.16 \pm 0.06$  for the high end and  $\alpha=2.05 \pm 0.09$  and  $C_1=0.09 \pm 0.02$  for the intermediate end. Note that the scale ratio over which these exponents were estimated is quite small due to numerical constraints and the attempt to simulate both scaling ranges. The graph also shows the ratio between high- and low-wavenumber  $K(q)$ , indicating that it has a slight  $q$  dependence, dropping from 1.7 ( $=H_z$ ) to approximately 1, roughly similarly to the data. (b)  $K_h(q)$  (circles) estimated from trace moments are simulations; triangles are data from the high-wavenumber regime. The simulations were with parameters  $\alpha=1.98$ ,  $C_1=0.08$ ,  $H_M=0.2$ ,  $H_z=1.7$ , the data for scales  $< 10$  km. We see that there is excellent agreement between the data and the simulations. The linear asymptote for  $q$  greater than about 3 is due to a multifractal phase transition (see text). (c)  $K_i(q)$  (circles) estimated from trace moments are simulations; triangles are data from the intermediate-wavenumber regime. The simulations were with parameters  $\alpha=1.98$ ,  $C_1=0.08$ ,  $H_M=0.2$ ,  $H_z=1.7$ , the data for scales  $> 10$  km. We see that there is excellent agreement between the data and the simulations. The linear asymptote for  $q$  greater than about 3 is due to a multifractal phase transition (see text).

Since we consider only 2-D (horizontal) fields, we will seek estimates of the exponents  $e, f, c$  in the horizontal generator

$$G_h = \begin{pmatrix} 1+c & f-e \\ f+e & 1-c \end{pmatrix}.$$

Note that  $\text{Trace}(G_h) = d_{e1}$  for the horizontal space has been set at a value of 2; this is equivalent to using the square root of areas of structures as the definition of scale (see the discussion in Paper I). The parameters were estimated using the scale-invariant generator technique (SIG; Lewis 1993; Lewis *et al.* 1999; for applications see Pecknold *et al.* 1997), which was used to determine the GSI parameters for the seven magnetic fields of data set #1. This technique is a least-squares regression method that is used to fit the generator of the anisotropy,  $G_h$ , to the spectral density  $P(k_x, k_y)$ . The basic technique is to minimize an error function  $E^2 = \int [P(\lambda^{-G_h \mathbf{k}}) - \lambda^{-s} P_{G_h}(\mathbf{k})]^2 d\mathbf{k}$ , where the minimization is with respect to both  $G_h$  parameters and spectral slope  $s$ . Since it uses the spectral slope as a parameter, this technique must first be altered so as to account for the break in scaling of the magnetic field power spectrum. One way to do this is to perform a minimization on areas of spectral density on either side of the break. Equivalently, the data sets can be ‘enhanced’ by filtering to eliminate the break. This technique consists of estimating the intermediate- and high-wavenumber spectral slopes and performing a fractional differentiation with differing order on each regime of the field, with the difference in order given by  $(\beta_i - \beta_h)/2$  (since theoretically  $\beta_i = s - 3$ ,  $\beta_h = s - 2$ , this difference = 1/2). One advantage of performing this is that it provides an enhancement of the higher-wavenumber structures of the field. This could be useful in the discovery of otherwise hidden magnetic anomalies. Fig. 10(a) shows an example of one of the data sets used, along with the 2-D power spectrum, with GSI balls given by the measured parameters (see Table 1) superimposed on it. The break in the spectrum in Fig. 10(b) has been compensated for by analysing the GSI parameters on the high- and low-wavenumber regimes.

The GSI parameters found for the data sets are listed in Table 2. If an isotropic scale exists (a true spheroscale; a circle in two dimensions), the size is given. In certain cases,

no spheroscale appears to exist; the simplest quadratic family (ellipses) does a poor job in this case. These systems can nevertheless be reasonably well described by a family of fourth-order polynomial balls, as described in Pecknold *et al.* (1996); in Table 2 these are the surveys marked ‘quartic’.

Note that in the majority of cases, we find  $a^2 < 0$ , hence the texture/morphology is rotation-dominant. In some extreme cases (e.g. the data set labelled ‘west’ in Table 2),  $a \approx 0.4i$ , implying a complete rotation of structures every factor of  $e^{2\pi/|a|} \approx 10^7$  in scale.

## 6.2 Horizontally anisotropic simulations

We now use the values obtained in the previous sections to perform simulations that include full horizontal anisotropy as well as the horizontal–vertical anisotropy. In the cases examined here, we assumed that there was no rotation of structures in the vertical plane; we expected (and found numerically) that the horizontal generator ( $G_h$ ) is the same for both  $\mathbf{M}$  and  $\mathbf{B}$ , hence the parameters  $c, e, f$  measured from the horizontal  $\mathbf{B}$  can be used directly in the  $\mathbf{M}$  simulation. Although these assumptions about  $\mathbf{M}$  do lead to correct simulated surface  $\mathbf{B}$  statistics, it is not obvious that completely neglecting rotations in the vertical plane is realistic. This question can only be answered by extensive empirical analysis of  $\mathbf{M}$  data.

As in the pure stratified cases, the multifractal parameters of the magnetization were  $\alpha = 1.98$ ,  $C_1 = 0.08$  and  $H = 0.2$ . The generator used was

$$\mathbf{G} = \begin{pmatrix} d+c & f-e & 0 \\ f+e & d-c & 0 \\ 0 & 0 & H_z \end{pmatrix},$$

with  $H_z = 1.7$ , a spheroscale of 5000 km and a Curie depth of 16 km. GSI parameters used were similar to those of data set nn141 (Table 2). Figs 11(a), 12(a) and 13(a) show simulated crustal magnetization for various horizontal anisotropies ( $G_h$ ), while Figs 11(b), 12(b) and 13(b) show the derived aeromagnetic fields. The basic morphological features—which are particularly visible in the  $\mathbf{B}$  fields—are various ‘textures’, some

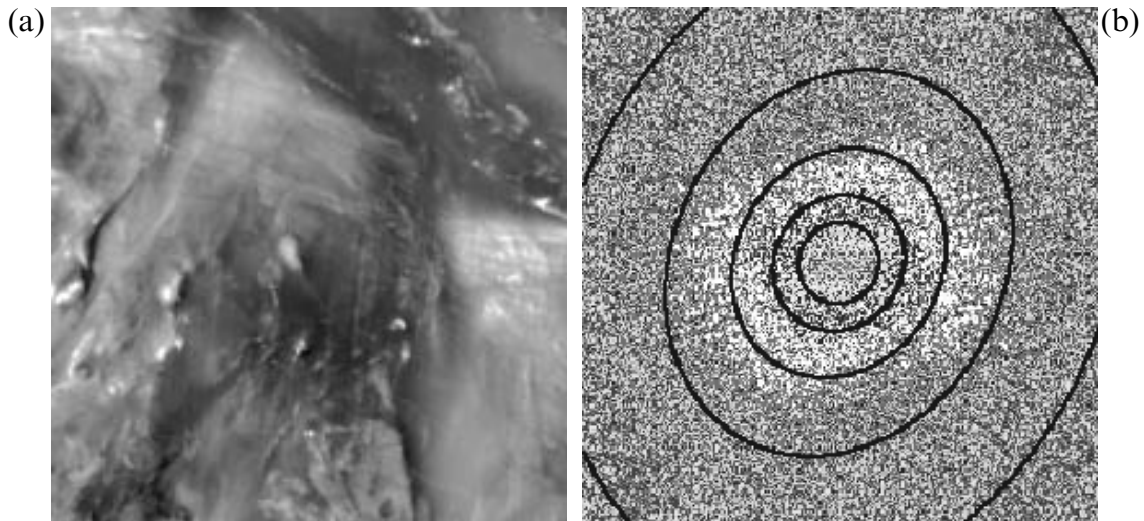


**Figure 10.** (a) Aeromagnetic field nn141 (left). The 2-D power spectrum  $P_B k_x, k_y$  with isolines fitted from calculated parameters:  $c = -0.01$ ,  $f = -0.05$ ,  $e = 0.20$ , horizontal spheroscale = 16.8 km.

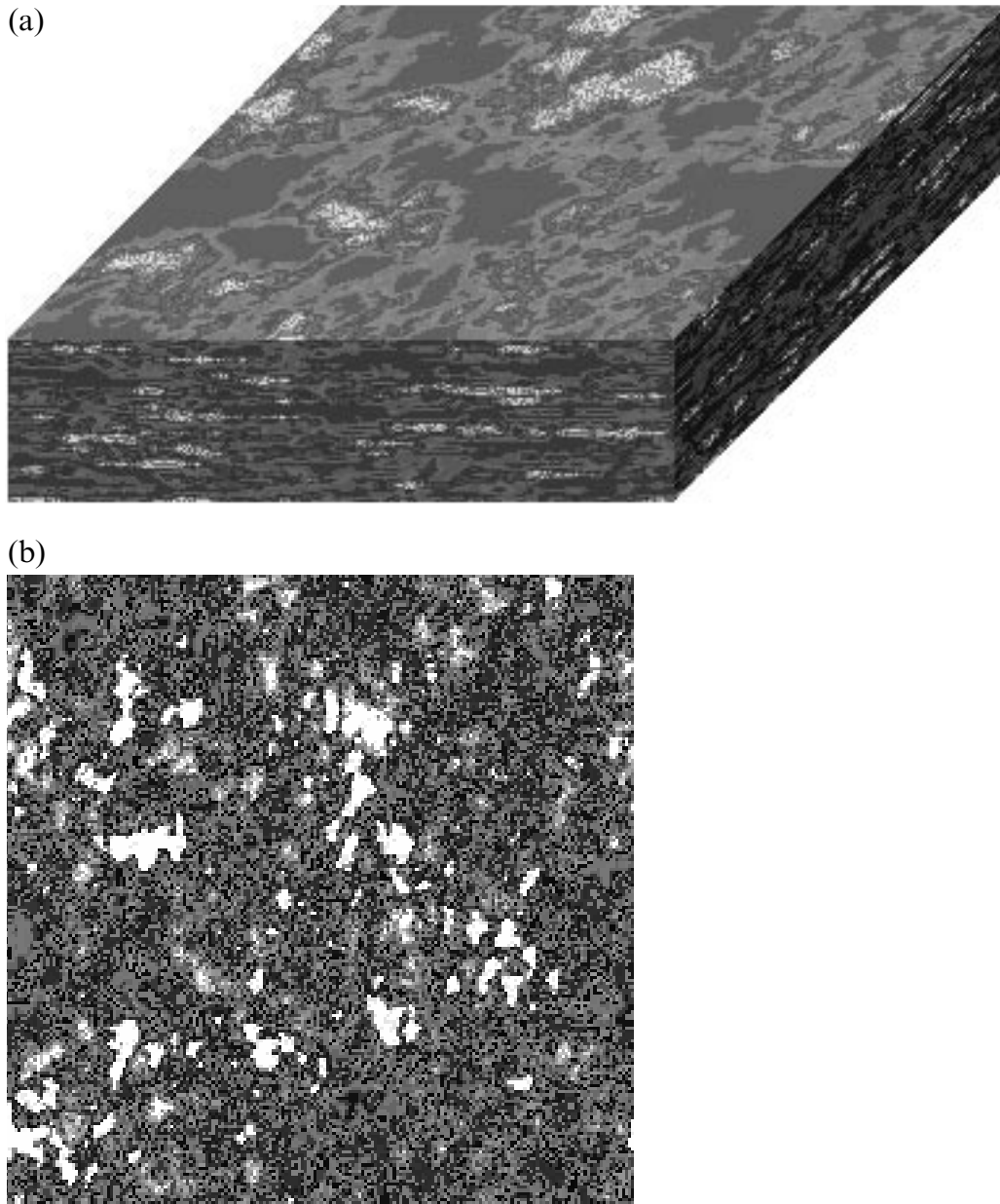


**Figure 11.** (a) Horizontally anisotropic  $\mathbf{M}$  field. The vertical anisotropy gives  $H_z=1.7$ ,  $s=4$ , with a spheroscale in the vertical plane of 2500 km, a spheroscale in the horizontal plane of 64 km and a Curie depth of 16 km. The horizontal anisotropy is  $c=0.07$ ,  $f=-0.04$ ,  $e=0.20$ ,  $d=1$ . The simulation is  $64 \times 64 \times 16$  km at 0.5 km resolution. (b) Magnetic field resulting from simulated crustal magnetization of (a).

of which resemble certain regions of the survey shown in Fig. 10(a). This is a basic limitation of linear GSI: it is only an approximation to the more general non-linear GSI presumably characteristic of the data. The full characterization and modelling of  $\mathbf{M}$ ,  $\mathbf{B}$  fields with non-linear GSI is an important subject for future research.

## 7 CONCLUSIONS

In Paper I, we argued that in order to account for the intermediate ‘red noise’ regime of the surface  $\mathbf{B}$  field (roughly 100 to 2000 km in scale) it was sufficient that models of  $\mathbf{M}$  and surface  $\mathbf{B}$  be scaling but anisotropic rather than self-similar. While this was sufficient for the spectral modelling presented in Paper I, it is only in the special case where the fields are quasi-

Gaussian that the spectrum gives a full statistical characterization of the process and its statistics. On the other hand, scaling fields (such as  $\mathbf{M}$ —or over various ranges—the surface  $\mathbf{B}$  field) define an infinite number of fractal sets, and hence they will generally require an infinite number of exponents (e.g. fractal dimensions) for their specification. Qualitatively, this multifractality corresponds to the various levels of activity/intensity, each having a different degree of sparseness (quantified by a fractal co-dimension). It allows for the existence of rare, violent (far from Gaussian) extreme events/anomalies (generally including non-classical algebraic probability tails; self-organized critical fluctuations). Finally, since stable, attractive universality classes exist for multifractal processes, most of the non-linear dynamical details generating the  $\mathbf{M}$  distribution are expected to be unimportant and the latter will generally be characterized

**Table 2.** Comparison of the generalized scale-invariant parameters for the surveys in data set #1. The parameters are believed to be accurate to roughly  $\pm 0.05$  (see Lewis 1993; Lewis *et al.* 1999). Note that in self-similar multifractals, all exponents would be zero. ‘Quartic’ refers to the fact that in some cases fourth-order polynomials were found to provide significantly better fits than the quadratics; in these cases no exactly isotropic scale exists.

Data set	$c$	$f$	$e$	$a$	Spheroscale
east	0.05	0.10	0.22	0.19 <i>i</i>	quartic
west	0.20	-0.14	-0.50	0.44 <i>i</i>	quartic
meg3	0.05	-0.10	0.10	0.05	100 m
nm151	-0.10	-0.30	-0.20	0.24	125 m
nn151	0.15	0.0	0.0	0.15	70 m
nn141	0.01	-0.05	0.20	0.19 <i>i</i>	16.8 km
no141	0.03	0.05	0.10	0.08 <i>i</i>	quartic

by three universal multifractal parameters. These universal behaviours includes the widespread geophysical log-normal phenomenology. Indeed, quasi-log-normality is *prima facie* evidence for universal multifractal statistics.

In Paper II, our goal was therefore to demonstrate and quantify the multifractality, and to use this information to produce multifractal models that—over as wide a range of scale and at each scale over the full range of intensities/statistical moments—would be as close to the observed  $\mathbf{M}$  and surface  $\mathbf{B}$  statistics as possible. Over the high and intermediate range of scales (i.e. out to about 2000 km), the dominant source of  $\mathbf{B}$  fluctuations was taken to be the  $\mathbf{M}$  in the crust. The main approximation was the assumption that  $\mathbf{B}$  and  $\mathbf{M}$  were parallel; in this range  $\mathbf{B}$  was therefore assumed to be primarily determined by the variations in susceptibility.  $\mathbf{M}$  is therefore fundamental while the surface  $\mathbf{B}$  is a (linearly) derived quantity.

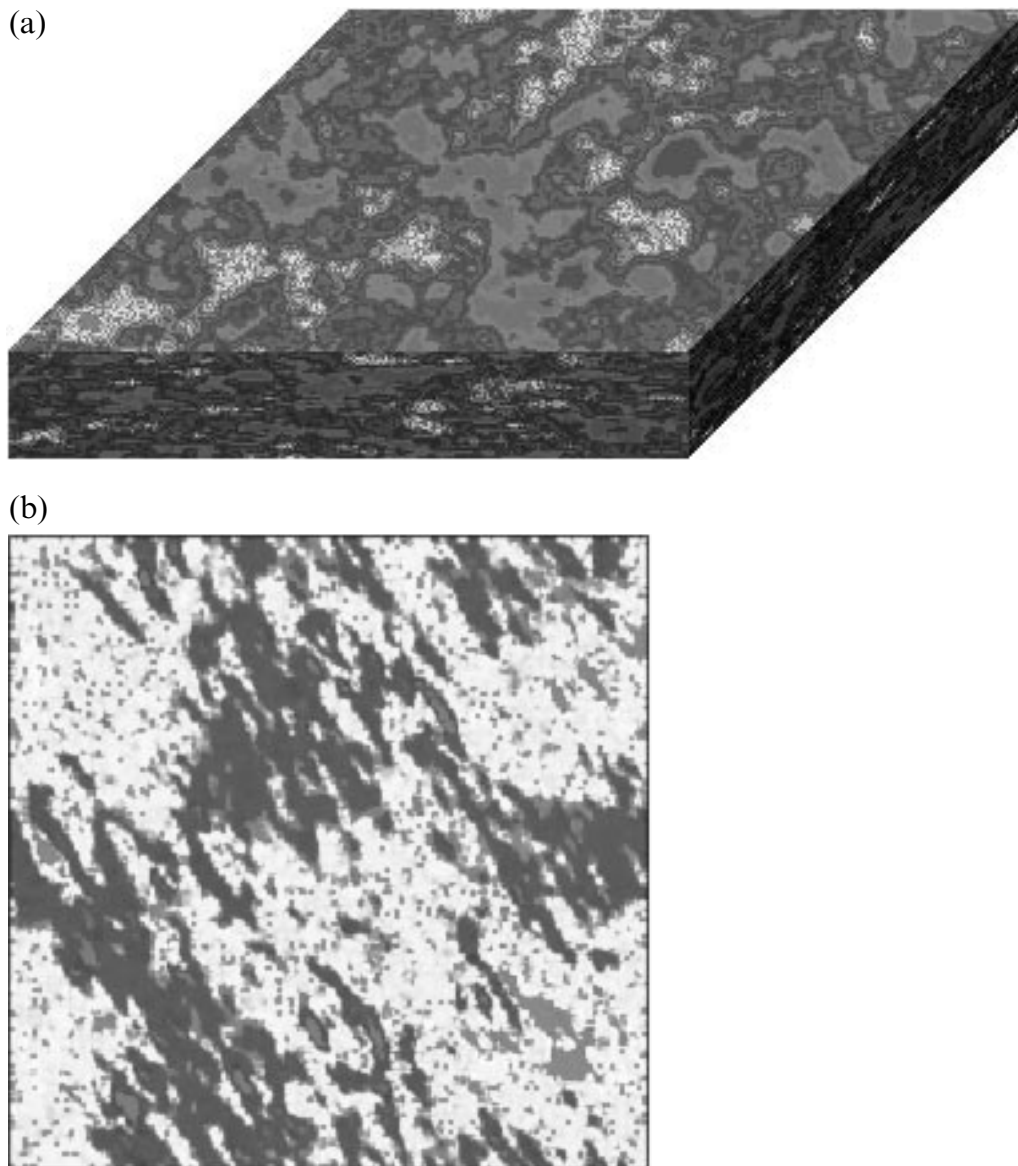


**Figure 12.** (a) Horizontally anisotropic  $\mathbf{M}$  field. The vertical anisotropy is given by  $H_z = 1.7$  with  $s = 4$ , with a spheroscale in the vertical plane of 2500 km (but only 64 km in the horizontal plane) and a Curie depth of 16 km. The horizontal anisotropy is determined by  $c = 0.1$ ,  $f = -0.05$ ,  $e = 0.15$ ,  $d = 1$ . The simulation is  $64 \times 64 \times 16$  km at 0.5 km resolution. (b)  $\mathbf{B}$  field resulting from simulated crustal  $\mathbf{M}$  of (a) (i.e. a region 64 km across). Note the preferred direction: the smaller-scale structures are elongated NW/SE, although since the horizontal spheroscale is 64 km, the effect is less pronounced at larger scales.

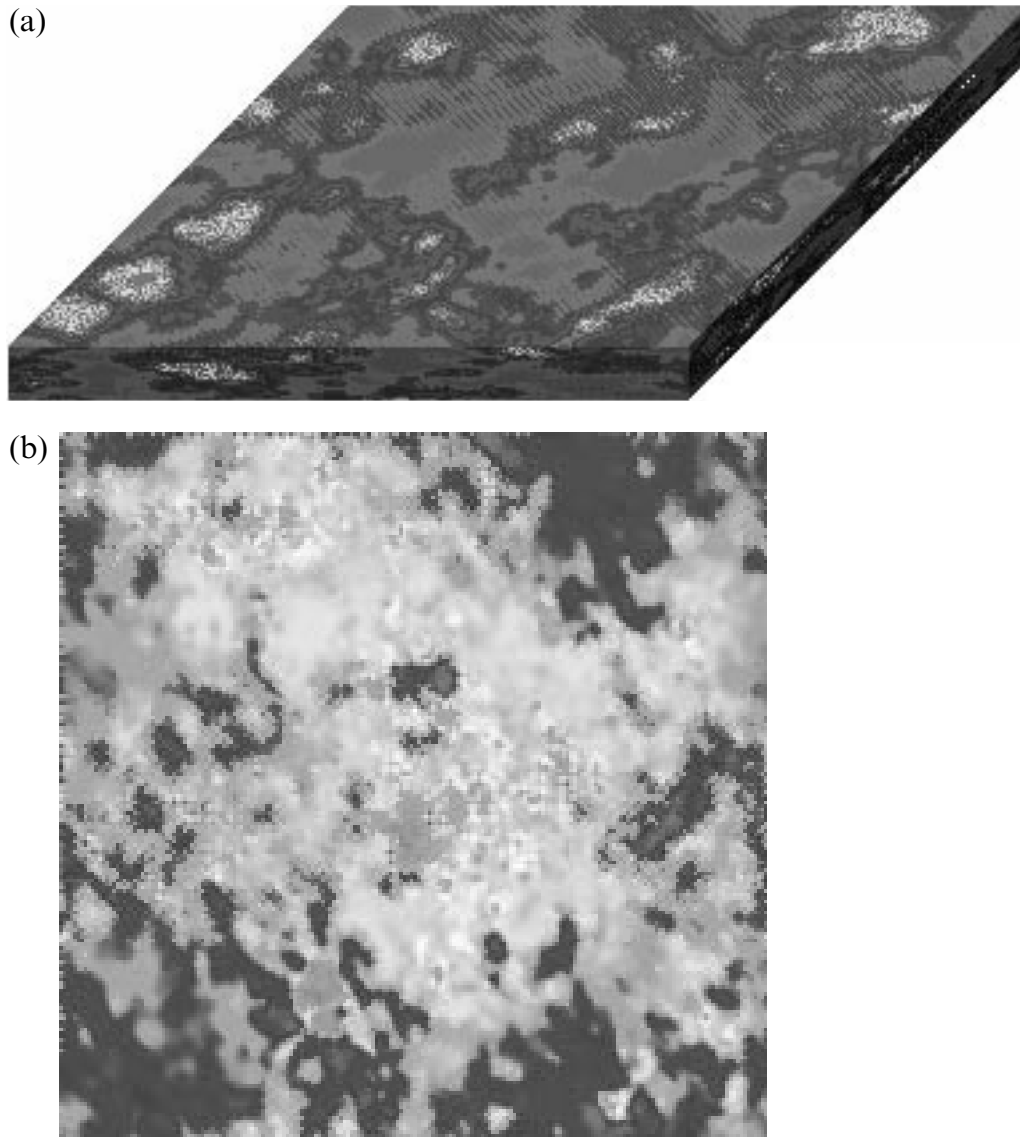


**Figure 13.** (a) Horizontally anisotropic  $\mathbf{M}$  field. The vertical anisotropy is given by  $H_z=1.7$  with  $s=4$ , with a spheroscale in the vertical plane of 2500 km (but only 64 km in the horizontal plane) and a Curie depth of 16 km. The horizontal anisotropy is determined by  $c=0.05$ ,  $f=0$ ,  $e=0.2$ ,  $d=1$ . The simulation is  $64 \times 64 \times 16$  km at 0.5 km resolution. (b)  $\mathbf{B}$  field resulting from simulated crustal  $\mathbf{M}$  of (a) (i.e. a region 64 km across). Note that although the differential rotation is stronger than in Figs 11(a) and (b) as quantified by the parameter  $e$ , the stratification parameters  $c$ ,  $f$  are very small so that although the ‘texture’ has changed with respect to a comparable horizontally isotropic field, e.g. Figs 7(a) and (b), there are no ‘striations’ such as those in Fig. 12(b).

The starting point for the multifractal model was thus a model of  $\mathbf{M}$ . However, the  $\mathbf{M}$  statistics are very poorly known; the best available evidence was from limited (surrogate) horizontal and vertical susceptibility spectra. The multifractal parameters were therefore estimated by a type of ‘bootstrap’ procedure, whereby the much better-quality surface  $\mathbf{B}$  data were used to deduce the  $\mathbf{M}$  statistics, and the multifractal model was used to check the overall procedure. The key was the fact that for the intermediate-range surface  $\mathbf{B}$ , the model showed that the basic multifractal exponents  $C_1$ ,  $\alpha$  were nearly the same as for the corresponding horizontal  $\mathbf{M}$  parameters. This, coupled with estimates of the stratification from Paper I [and also from the ratio of high- and intermediate-wavenumber surface  $\mathbf{B}$  exponents  $K_h(0)/K_i(0)$ ], provided the following estimate of the universal multifractal  $\mathbf{M}$  parameters:  $C_{1M}=0.08$ ,  $\alpha=1.98$  and  $H_M=0.2$ . Since the value  $\alpha=2$  corresponds to Gaussian generators and

(near) log-normal statistics, this result is roughly compatible with the log-normal fits of Pilkington & Todoeschuk (1993). The resulting magnetization spectra in the horizontal and vertical were very close to the susceptibility spectra, whereas the high- and intermediate-wavenumber surface  $\mathbf{B}$  statistics of all orders (i.e. including those of second order, the spectra) were found to be very close to those observed. In addition, the simulations had plausible visual appearances, including stratification and anomalies.

Since there is no reason to expect horizontal isotropy we also investigated the anisotropic nature of the surface  $\mathbf{B}$  field using the scale-invariant generator technique to estimate the best linear approximation to the generator of the scale-changing operator. The parameters of the horizontal anisotropy are associated with different morphologies and textures and enabled us to simulate  $\mathbf{B}$  fields numerically; their values—typically of the order of

0.2–0.3 ± 0.05—are sufficiently far from the isotropic value 0 to exclude horizontal self-similarity. In the case examined here, we assumed that there was no rotation of structures in the vertical plane, hence the horizontal generator ( $G_h$ ) is the same for both  $\mathbf{M}$  and  $\mathbf{B}$ . This, together with the parameters provided by the multifractal analysis and the 3-D anisotropy of the magnetization, provided the information necessary to perform quite realistic simulations of magnetization and aeromagnetic anomaly fields. These simulations reinforced our model of multifractal anisotropic magnetization: in addition to realistic ‘textures’, the derived fields exhibited scaling and multifractal characteristics very similar to those found in the data.

Although scaling ideas have penetrated many solid earth geophysics subfields (see e.g. the early reviews in Turcotte 1992; Korvin 1992), they have unfortunately generally been in the simplistic form of self-similar fractal geometry. In this two-part series of papers, we have argued that geophysics is both multiscaling and anisotropic, so that realistic applications will require the kind of anisotropic multifractal framework used here. Although we have shown how such models can be used in finding new approaches to solving potential problems, we anticipate that they will become indispensable tools in other geophysical inversion problems where realistic statistical constraints are theoretically necessary. Similarly, by providing new data analysis tools (such as trace moments)—going well beyond spectral analysis—a clearer characterization of the scale-by-scale and intensity-by-intensity variability of geophysical fields will gradually be achieved.

## ACKNOWLEDGMENTS

We thank F. Francis, T. Falco and C. Hooge for help with some of the data analysis. M. Pilkington is especially thanked for supplying the magnetic survey data as well as the spectra from several of his publications. He also participated in many helpful discussions about the interpretation of aeromagnetic surveys and suggested many useful references. We thank J. Todoschuk for long discussions and for critically commenting on an earlier draught. We also thank a referee (Prof. A. De Santis) for valuable suggestions for improving the manuscript. The Canadian Geological Commission is thanked for partial financial support.

## REFERENCES

- Addor, J.B., Lovejoy, S. & Schertzer, D., 2000. Quantifying cloud texture and morphology using generalized scale invariance, *Int. Conf. on Clouds and Precipitation*, Reno, USA.
- de Wisj, H.J., 1951. Statistics of ore distributions. Part I: frequency distributions of assay values, *Geol. Mijnb.*, **13**, 365–375.
- Frisch, U.P., Sulem, P.L. & Nelkin, M., 1978. A simple dynamical model of intermittency in fully developed turbulence, *J. Fluid Mech.*, **87**, 719–724.
- Korvin, G., 1992. *Fractal Models in the Earth Sciences*, Elsevier, Amsterdam.
- Lavallée, D., Lovejoy, S., Schertzer, D. & Schmitt, F., 1992. On the determination of universal multifractal parameters in turbulence, in *Topological Aspects of the Dynamics of Fluids and Plasmas*, pp. 463–478, eds Moffat, K., Tabor, M. & Zaslavsky, G., Kluwer, Dordrecht.
- Lavallée, D., Lovejoy, S., Schertzer, D. & Ladoy, P., 1993. Nonlinear variability and landscape topography: analysis and simulation, in *Fractals in Geography*, pp. 171–205, eds De Cola, L. & Lam, N., Prentice Hall, Englewood Cliffs, NJ.
- Lewis, G., 1993. The scale invariant generator technique and scaling anisotropy in geophysics, *MSc thesis*, McGill University, Montréal.
- Lewis, G., Lovejoy, S., Schertzer, D. & Pecknold, S., 1999. The scale invariant generator technique for parameter estimates in generalized scale invariance, *Comp. Geosci.*, **25**, 963–978.
- Lovejoy, S. & Schertzer, D., 1990. Our multifractal atmosphere: a unique laboratory for non-linear dynamics, *Can J. Phys.*, **46**, 62.
- Lovejoy, S. & Schertzer, D., 1995. How bright is the coast of Brittany?, in *Fractals in Geoscience and Remote Sensing*, pp. 102–151, ed. Wilkinson, G., Office for Official Publications of the European Communities, Luxembourg.
- Lovejoy, S. & Schertzer, D., 1998. Stochastic chaos and multifractal geophysics, in *Chaos, Fractals and Models 96*, pp. 38–52, eds Guindani, F.M. & Salvadori, G., Italian University Press, Pavia.
- Lovejoy, S. & Schertzer, D., 1999. Stochastic chaos, symmetry and scale invariance, *ECO-TEC: Architecture of the In-between*, pp. 80–99, ed. Marras, A., Princeton Architectural Press, Princeton, NJ.
- Lovejoy, S., Schertzer, D. & Stanway, J.D., 2001a. Direct evidence of atmospheric cascades from planetary scales down to 1 km, *Phys. Rev. Lett.*, submitted.
- Lovejoy, S., Gaonac’h, H., Mareschal, J.C., Bourlon, E. & Schertzer, D., 2001b. Anisotropic multiscaling models of rock density and the earth’s surface gravity field, *J. geophys. Res.*, in preparation.
- Lovejoy, S., Schertzer, D., Tessier, Y. & Gaonac’h, H., 2001c. Multifractals and resolution independent remote sensing algorithms: the example of ocean colour, *Int. J. Rem. Sens.*, in press.
- Mandelbrot, B.B., 1974. Intermittent turbulence in self-similar cascades: divergence of high moments and dimension of the carrier, *J. Fluid Mech.*, **62**, 331–350.
- Mandelbrot, B., 1977. *Fractals: Form, Chance and Dimension*, W. H. Freeman, San Francisco.
- Marsan, D. & Bean, J.C., 1999. Multiscaling nature of sonic velocities and lithography in the upper crystalline crust: evidence from the KTB main borehole, *Geophys. Res. Lett.*, **26**, 275–278.
- Marsan, D., Schertzer, D. & Lovejoy, S., 1996. Causal space-time multifractal processes: predictability and forecasting of rain fields, *J. geophys. Res.*, **31D**, 26 333–26 346.
- Monin, A.S. & Yaglom, A.M., 1975. *Statistical Fluid Mechanics*, MIT press, Boston, MA.
- Novikov, E.A. & Stewart, R., 1964. Intermittency of turbulence and spectrum of fluctuations in energy-dissipation, *Izv. Akad. Nauk. SSSR. Ser. Geofiz.*, **3**, 408–412.
- Parisi, G. & Frisch, U., 1985. A multifractal model of intermittency, in *Turbulence and Predictability in Geophysical Fluid Dynamics and Climate Dynamics*, pp. 84–88, eds Ghil, M., Benzi, R. & Parisi, G., North Holland, Amsterdam.
- Pecknold, S., Lovejoy, S., Schertzer, D., Hooge, C. & Malouin, J.F., 1993. The simulation of universal multifractals, in *Cellular Automata: Prospects in Astrophysical Applications*, pp. 228–267, eds Perchang, J.M. & Lejeune, A., World Scientific, Singapore.
- Pecknold, S., Lovejoy, S. & Schertzer, D., 1996. The morphology and texture of anisotropic multifractals using generalized scale invariance, in *Stochastic Models in Geosystems*, pp. 269–312, Molchanov, S. & Woyczynski, W., Springer-Verlag, New York.
- Pecknold, S., Lovejoy, S., Schertzer, D. & Hooge, C., 1997. Multifractals and the resolution dependence of remotely sensed data: generalized scale invariance and geographical information systems, in *Scaling in Remote Sensing and Geographical Information Systems*, pp. 361–394, eds Quattrochi, D. & Goodchild, M., Lewis, Boca Raton.
- Pilkington, M. & Todoschuk, J.P., 1993. Fractal magnetization of continental crust, *Geophys. Res. Lett.*, **20**, 627–630.
- Richardson, L.F., 1922. *Weather Prediction by Numerical Process*, Cambridge University Press, Cambridge (republished by Dover, 1965).

- Sachs, D., Lovejoy, S. & Schertzer, D., 2001. The multifractal scaling of cloud radiances from 1m to 1km, *Fractals*, in press.
- Schertzer, D. & Lovejoy, S., 1985. The dimension and intermittency of atmospheric dynamics, in *Turbulent Shear Flows*, Vol. 4., pp. 7–33, ed. Launder, B., Springer, Berlin.
- Schertzer, D. & Lovejoy, S., 1987. Physical modeling and analysis of rain and clouds by anisotropic scaling of multiplicative processes, *J. geophys. Res.*, **D88**, 9693–9714.
- Schertzer, D. & Lovejoy, S., 1991. Scaling nonlinear variability in geodynamics, in *Nonlinear Variability in Geophysics: Scaling and Fractals*, pp. 41–82, Schertzer, D. & Lovejoy, S., Kluwer, Dordrecht.
- Schertzer, D. & Lovejoy, S., 1992. Hard and soft multifractal processes, *Physica A*, **185**, 187–194.
- Schertzer, D. & Lovejoy, S., 1994. Multifractal generation of self-organized criticality, in *Fractals in the Natural and Applied Sciences*, pp. 325–339, ed Novak, M.M., Elsevier, North-Holland, Amsterdam.
- Schertzer, D.S. & Lovejoy, 1997. Universal multifractals do exist!: Comments on 'A statistical analysis of mesoscale rainfall as a random cascade', *J. appl. Meteor.*, **36**, 1296–1303.
- Schertzer, D., Lovejoy, S. & Schmitt, F., 1995. Structures in turbulence and multifractal universality, in *Small-Scale Structures in 3D and MHD Turbulence*, pp. 137–144, eds Meneguzzi, M., Pouquet, A. & Sulem, P.L., Springer-Verlag, New York.
- Schertzer, D., Lovejoy, S., Schmitt, F., Chigirinskaya, Y. & Marsan, D., 1997. Multifractal cascade dynamics and turbulent intermittency, *Fractals*, **5**, 427–471.
- Turcotte, D.L., 1992. *Fractals and Chaos in Geology and Geophysics*, Cambridge University Press, Cambridge.
- Veneziano, D. & Iacobellis, V., 1999. Self-similarity and multifractality of topographic surfaces at basin and subbasin scales, *J. geophys. Res.*, **104**, 12 797–12 812.
- Weissel, J.K. & Pratson, L.F., 1994. The length scaling properties of topography, *J. geophys. Res.*, **99**, 13 997–14 012.
- Wilson, J., Lovejoy, S. & Schertzer, D., 1991. Physically based cloud modelling by scaling multiplicative cascade processes, in *Scaling, Fractals and Non-linear Variability in Geophysics*, pp. 185–208, eds Schertzer, D. & Lovejoy, S., Kluwer, Dordrecht.
- Yaglom, A.M., 1966. The influence on the fluctuation in energy dissipation of the shape of turbulent characteristics in the inertial interval, *Sov. Phys. Dokl.*, **2**, 26–30.